BNL-102610-2013-TECH
BNL-102610-2013-IR

Large-Grain Superconducting Gun Cavity Testing Program Phase One Closing Report

L. Hammons

October 2013

Collider Accelerator Department
Brookhaven National Laboratory

U.S. Department of Energy
USDOE Office of Science (SC)

Notice: This technical note has been authored by employees of Brookhaven Science Associates, LLC under Contract No.DE-AC02-98CH10886 with the U.S. Department of Energy. The publisher by accepting the technical note for publication acknowledges that the United States Government retains a non-exclusive, paid-up, irrevocable, world-wide license to publish or reproduce the published form of this technical note, or allow others to do so, for United States Government purposes.

DISCLAIMER

This report was prepared as an account of work sponsored by an agency of the United States Government. Neither the United States Government nor any agency thereof, nor any of their employees, nor any of their contractors, subcontractors, or their employees, makes any warranty, express or implied, or assumes any legal liability or responsibility for the accuracy, completeness, or any third party's use or the results of such use of any information, apparatus, product, or process disclosed, or represents that its use would not infringe privately owned rights. Reference herein to any specific commercial product, process, or service by trade name, trademark, manufacturer, or otherwise, does not necessarily constitute or imply its endorsement, recommendation, or favoring by the United States Government or any agency thereof or its contractors or subcontractors. The views and opinions of authors expressed herein do not necessarily state or reflect those of the United States Government or any agency thereof.

BNL-102610-2013-IR

C-A/AP/494
October 2013

Large-Grain Superconducting Gun Cavity Testing Program Phase One Closing Report

L. Hammons
On behalf of the Large-Grain Cavity Testing Project Team

Collider-Accelerator Department
Brookhaven National Laboratory
Upton, NY 11973

Notice: This document has been authorized by employees of Brookhaven Science Associates, LLC under Contract No. DE-AC02-98CH10886 with the U.S. Department of Energy. The United States Government retains a non-exclusive, paid-up, irrevocable, world-wide license to publish or reproduce the published form of this document, or allow others to do so, for United States Government purposes.

Large-Grain Superconducting Gun Cavity Testing Program

Phase One Closing Report

L. Hammons

On behalf of the Large-Grain Cavity Testing Project Team:

S. Bellavia, S. Belomestnykh, I. Ben-Zvi, C. Cullen, J. Dai, C. Degen, H. Hahn, L. Masi, G. McIntyre, C. Schultheiss, T. Seda, R. Kellerman, T. Tallerico, R. Todd, S. Tuozzolo, W. Xu, Y. Than

October 2013

Contents

Abstract

This report details the experimental configuration and RF testing results for the first phase of a large-grained niobium electron gun cavity testing program being conducted in the Small Vertical Testing Facility in the Collider-Accelerator Department. This testing is meant to explore multipacting in the cavity and shed light on the behavior of a counterpart cavity of identical geometry installed in the Energy Recovery LINAC being constructed in the Collider-Accelerator Department at Brookhaven National Laboratory.

This test found that the Q of the large-grained cavity at 4 K reached ~6.5×10^8 and at 2 K reached a value of ~6×10^9. Both of these values are about a factor of 10 lower than would be expected for this type of cavity given the calculated surface resistance and the estimated geometry factor for this half-cell cavity. In addition, the cavity reached a peak voltage of 0.6 MV before there was significant decline in the Q value and a substantial increase in field emission. This relatively low voltage, coupled with the low Q and considerable field emission suggest contamination of the cavity interior, possibly during experimental assembly. The results may also suggest that additional chemical etching of the interior surface of the cavity may be beneficial.

Throughout the course of testing, various challenges arose including slow helium transfer to the cryostat and cable difficulties. These difficulties and others were eventually resolved, and the report discusses the operating experience of the experiment thus far and the plans for future work aimed at exploring the nature of multipacting with a copper cathode inserted into the cavity.

1 Project Scope

This report describes the progress to date on a testing program for a superconducting, large-grain niobium electron gun cavity designed for use in the Energy Recovery LINAC (ERL) being constructed in the Collider-Accelerator Department at Brookhaven National Laboratory. The goal of the testing program is to characterize the RF properties of the gun cavity at superconducting temperatures, and, in particular, to study multipacting that is suspected to be occurring in the choke joint of the cavity into which a rod is inserted whose tip is covered by a semiconducting material designed to emit electrons when exposed to laser light. The rod is referred to as a photocathode, and the insertion process is designed to be conducted hermetically in order to preserve the particulate-free cleanliness of the interior of the superconducting cavity. Furthermore, the design of the double-quarter-wave choke joint is supposed to trap and contain RF fields that may escape through the insertion port of the cavity as well as suppress multipacting through a unique grooved surface [1]. A schematic of the cavity is shown in Figure 1.1.

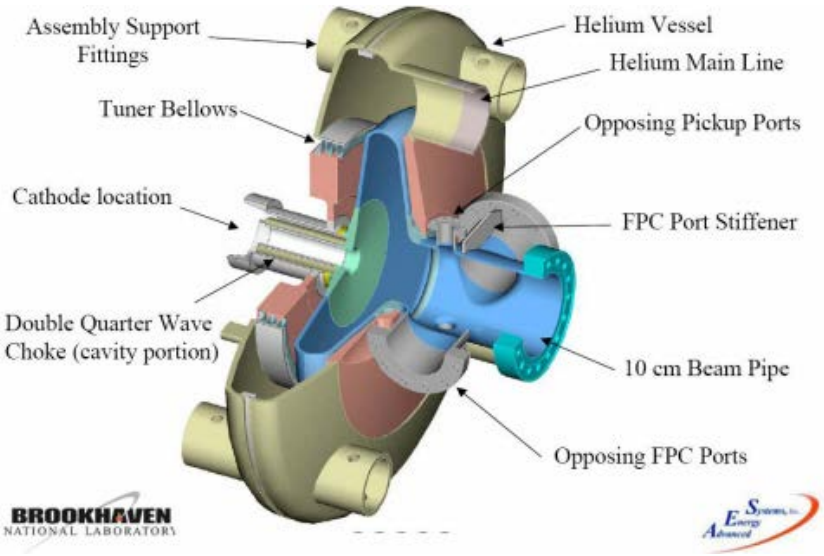

Figure 1.1 – Superconducting RF gun with double-quarter-wave choke joint shown on left.

These efforts were motivated by the multipacting issues that were observed in the processing of a fine-grained niobium cavity with the same geometry at Jefferson Laboratory several years ago. Given that the goal of the processing efforts was to achieve gradients of at least 20 MV/m, the observed multipacting had caused significant concern.

The multipacting is believed to be occurring in the choke joint of the gun cavity. It is suspected that the chemical processing may have affected the geometry of this region and the fine groove structure making it more susceptible to multipacting. Several previous studies have attempted to characterize the geometry of the grooves [2] as well as simulate the multipacting due to the altered geometry [3]. The simulation study, in particular, has shown results that agree with the observed behavior at Jefferson Laboratory, and, therefore, the present work on the large-grain cavity is motivated by the desire to pinpoint the sites of multipacting on the altered geometry as well as determine how a pristine cavity and photocathode insert, unaltered by the chemistry, might behave.

The fine-grain niobium gun cavity has been installed in the ERL and will serve as the photoinjector for the accelerator, while the large-grain gun, which is identical in every aspect of construction and geometry shall serve as a spare gun cavity for the ERL program. The only intrinsic difference between the two gun cavities is the niobium material of which they are constructed, one having grain boundaries that are finely spaced and the other having grain boundaries that are relatively far apart, making for large grains that are clearly visible. Figure 1.2 shows a picture of the cavity.

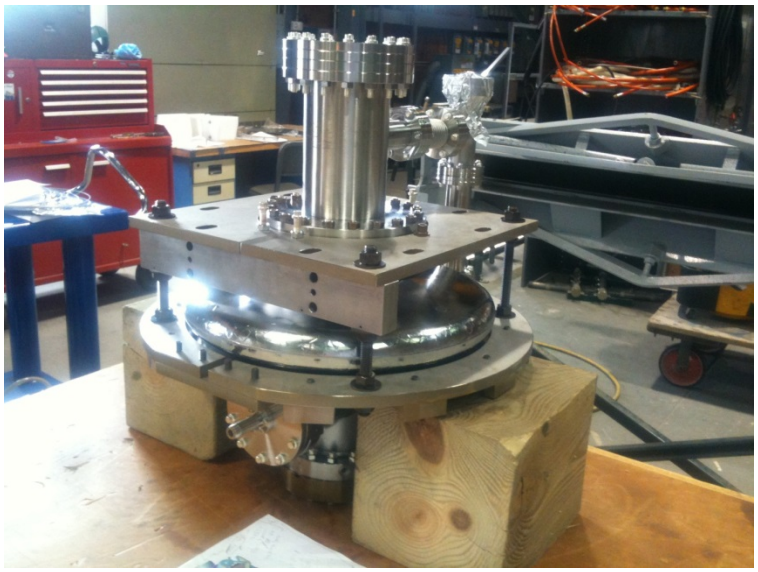

Figure 1.2 – Picture of large-grain cavity in vacuum restraint.

As the fine-grain cavity was being processed, multipacting was encountered at a gradient of approximately 3 MV/m. This multipacting resisted all efforts at elimination and unanswered questions about the origin and nature of this multipacting remain that the testing program for the large-grain electron gun was designed to answer.

The testing program is divided into three stages:

1. Low-Power Testing at Superconducting Temperatures Without a Test-Cathode Insert

   This stage is necessary to configure and verify the experimental setup and includes Q and S-parameter measurements of the gun at low to medium power (20-200 W) at superconducting temperatures (2 and 4 K). The experimental apparatus for the project will be designed in this stage, including the fundamental power couplers to be used throughout the project, the motion control system for the power coupler, the suspension system for the cavity in the cryostat, and a camera system for visual inspection of the choke among other items. This juncture in the project lifecycle sets the stage for all of the subsequent experimental activities. In this stage, no significant multipacting is expected.

2. Testing at Superconducting Temperatures with a Niobium Test-Cathode Insert

   In this stage, testing will proceed at superconducting temperatures using a 200 W amplifier. Q and power measurements of the gun will be conducted. In addition, a niobium cathode insert specially designed for vertical cavity testing only and which approximates the photocathode but without the photoemissive material will be inserted into the choke joint of the gun. The addition of the niobium cathode insert is important in this stage since it possesses the geometrical properties and processing history that are suspected to be implicated in the multipacting that has been observed in the fine-grain gun.

3. Testing at Superconducting Temperatures with a Copper Test-Cathode Insert

   In this stage, testing will proceed at superconducting temperatures using a 200 W amplifier with a copper test cathode. The copper insert is formed in such a manner as to resemble the geometry of the niobium insert but will be spared the chemical processing that the niobium insert has already undergone so that the geometry will remain pristine and unaltered by chemistry. In this manner, the effects of the geometry and the change of material on the nature of the multipacting can be studied. Q and power data will be collected from this stage as well.

2 Experimental Design

This report documents the progress of the first stage of the testing program: low-power testing of the cavity at superconducting temperatures. The results of this testing effort will be described including the voltage and Q-value obtained along with a description of the apparatus, testing methods, and lessons learned from this stage of the test program that will be applied to subsequent testing activities. In addition, an outline of the future testing program will be described.

2.1 Superconducting RF Cavity

The large-grain niobium superconducting RF gun cavity is a ½-cell structure that is designed to operate at 703.75 MHz. The motivation and details of its design have been described in great detail in a number of sources and shall not be reiterated here except for those features that have bearing on the present study [4] –[6]. As was mentioned above, the large-grain niobium used for this gun distinguishes this cavity from its fine-grain counterpart that is being used in the ERL. Otherwise, the geometry of the two guns is exactly the same, and the large-grain niobium is not expected to have any direct impact on the RF properties of the gun.

2.2 Chemical Processing

Chemical processing was conducted at Jefferson Lab to prepare the cavity for testing. The cavity had never been subjected to chemical processing beforehand, and the structure was subjected to a modified version of Jefferson Lab's C100 process. Namely, the process flow included the following:

1. RF frequency measurements warm
2. Thickness measurements
3. Degrease
4. BCP 140 μm
5. Thickness measurements
6. Degrease
7. Heat Treat 600° C for 10 hours
8. Degrease
9. Light BCP 20 μm
10. HPR
11. Assembly - no VTA cathode

2.3 Fundamental Power Coupler Design

The fundamental power coupler (FPC) was a key design feature of the project, and two different designs were conceived: a low-power fixed, coaxial design and a design intended for higher-power, variable-position operation. During the course of work, the low-power design was not employed because an FPC coupler that had been designed and used at Jefferson Laboratory was already in place, and it was deemed unnecessary to open the cavity and insert the low-power coupler. Nonetheless, a schematic of the design is included for reference in Figure 2.1.

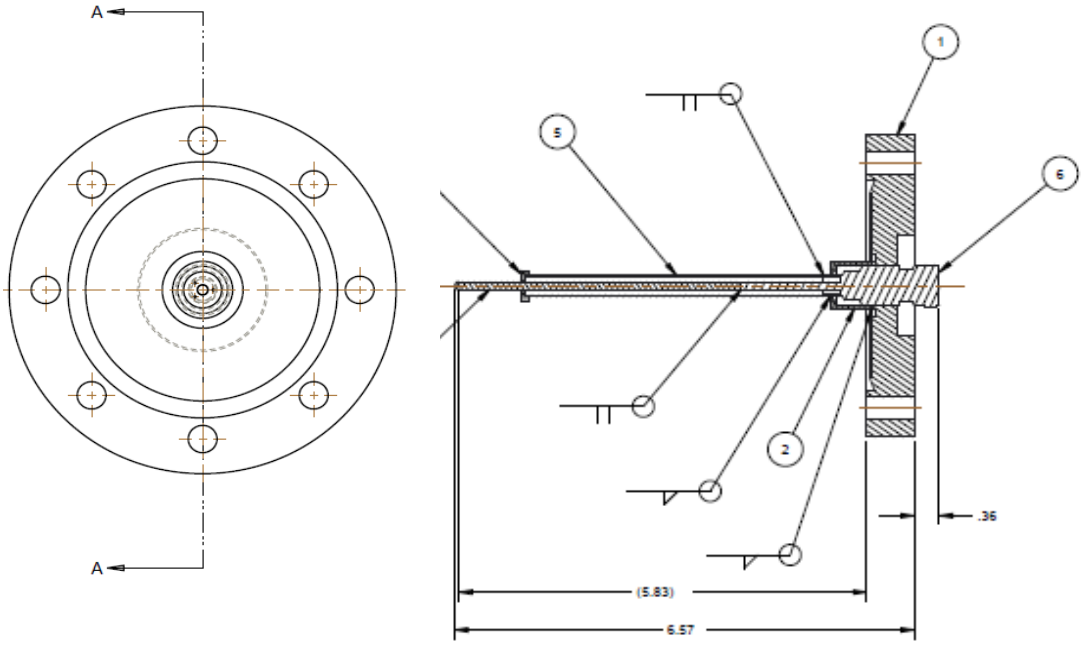

Figure 2.1 - Low-power coupler designed for use in the large-grain cavity.

2.4 High-Power Variable Coupler

After initial testing using the coupler that had been supplied with cavity by Jefferson Laboratory, the high-power, variable-position coupler was installed and used for the remainder of testing in the cavity. This coupler was designed to sustain higher power (200 W CW and up to 10 kW pulsed) and allows for the position of the coupler to be varied in the cavity to make operation at critical coupling possible at a variety of different power levels in real-time. The calculated input power required for critical coupling to achieve critical coupling for various voltage levels in the cavity is summarized in Figure 2.2.

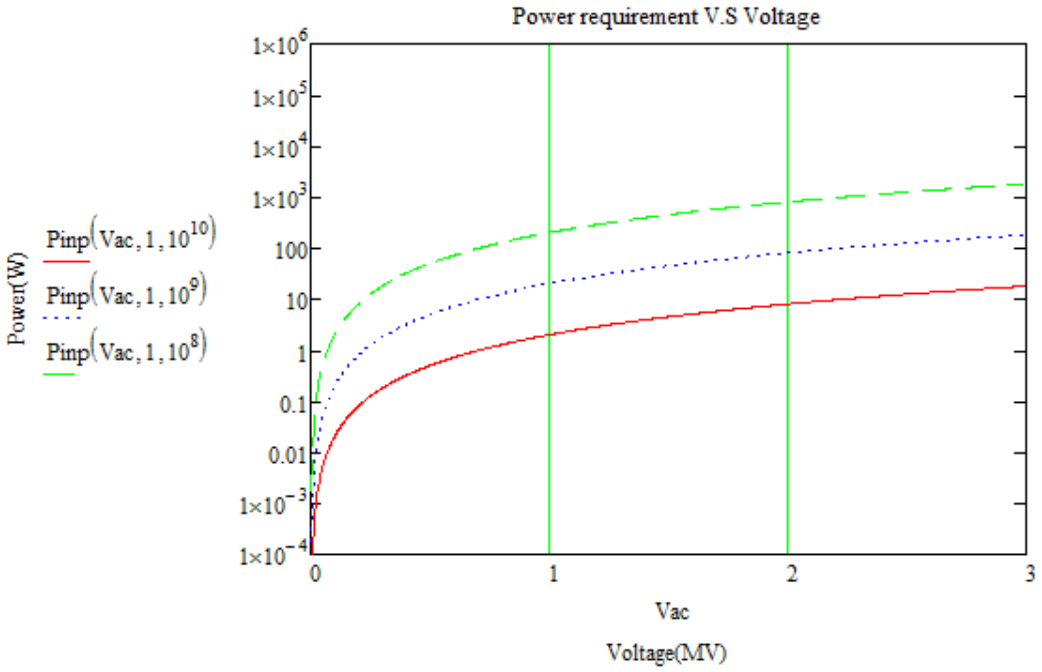

Figure 2.2 - Plot of input power vs. voltage for critical coupling at several different values of Q_0. The red solid curve represents a Q_0 value of 10^{10} expected at a temperature of 2 K. The green dashed curve represents a Q_0 value of 10^8 expected at 4 K. The blue dotted curve represents an intermediate Q_0 value of 10^9. Note that the goal cavity voltage is 2 MV. Therefore, 8 W of input power is expected to achieve 2 MV at 2 K and 800 W is expected to be required to achieve 2 MV at 4 K.

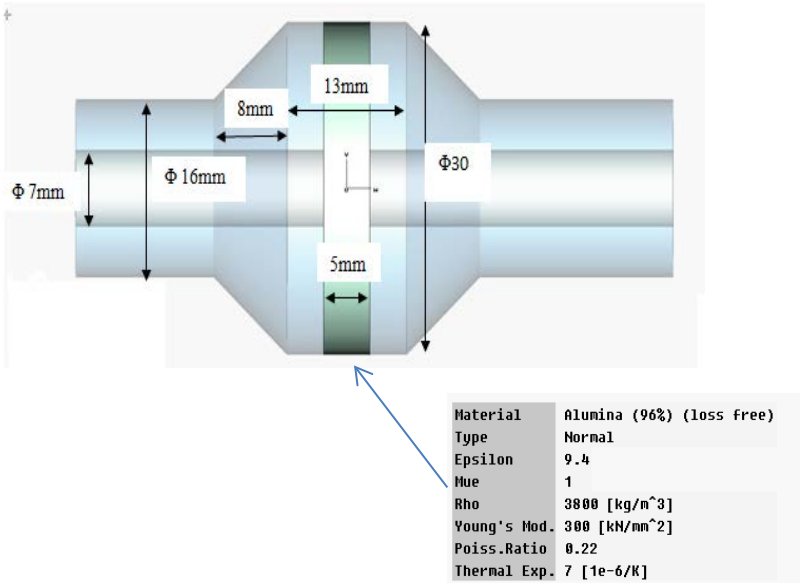

Figure 2.3 - Schematic of dimensions of RF feedthrough. The green section is alumina, and the properties of the alumina section used for simulation purposes are summarized in the call-out below.

The coupler antenna itself is similar in design to the low-power coupler, except that it used a custom feedthrough designed by W. Xu for broadband RF transmission with minimum reflection and manufactured by MPF Products, Inc. A summary of the mechanical properties is presented in Figure 2.3 and Figure 2.4. The RF properties of the feedthrough are presented in Figure 2.5 and Figure 2.6.

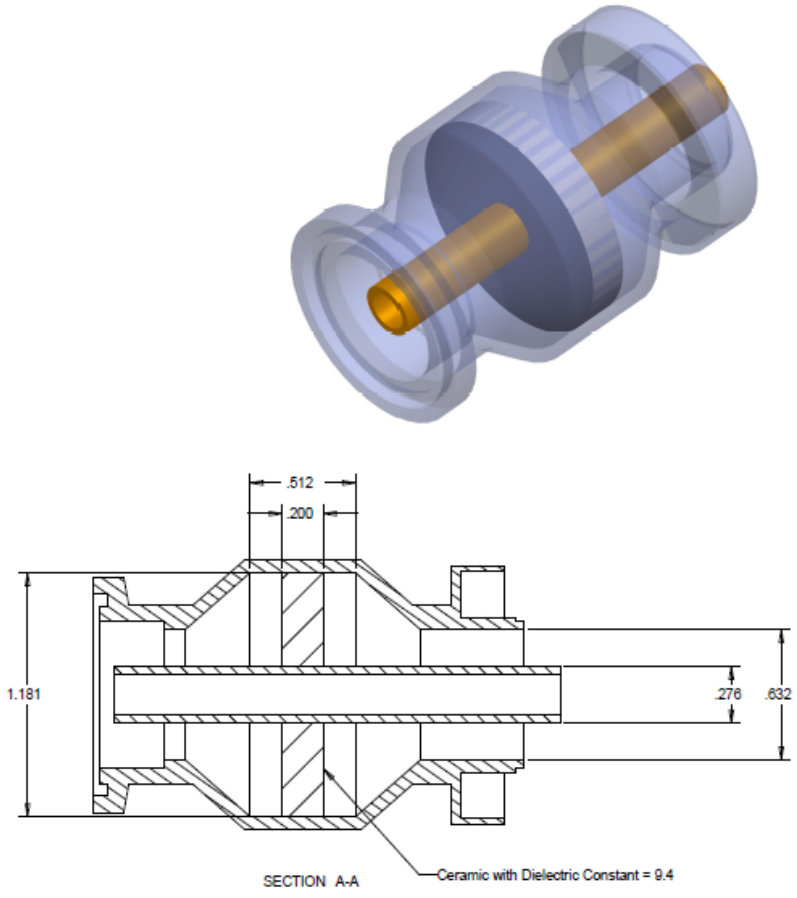

Figure 2.4 - Dimensions of the RF feedthrough as manufactured by MPF Products, Inc.

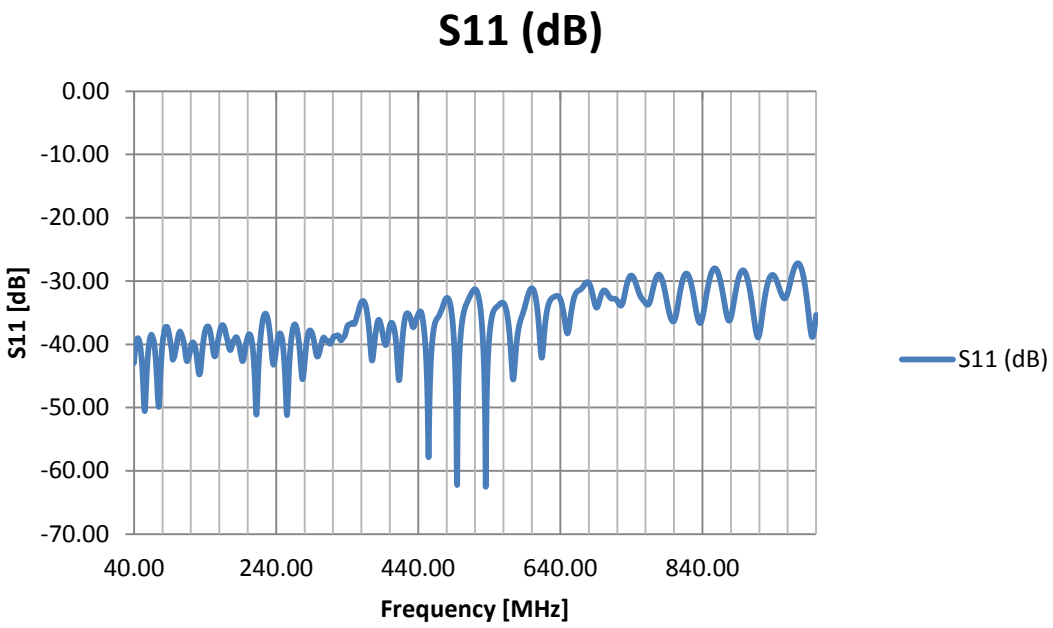

Figure 2.5 - S_{11} measurement results for the RF feedthrough for frequencies between 40 MHz and 1 GHz. Broadband reflection is less than -26 dB throughout the entire range.

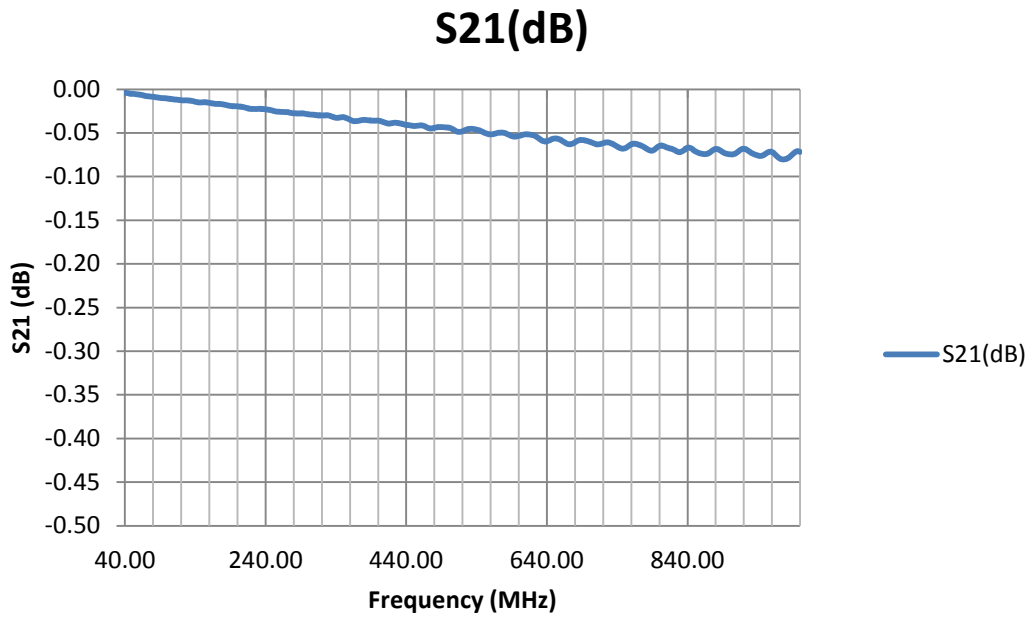

Figure 2.6 - S_{21} measurement results for the RF feedthrough between 40 MHz and 1 GHz. Transmission is better than -0.1 dB throughout the entire range.

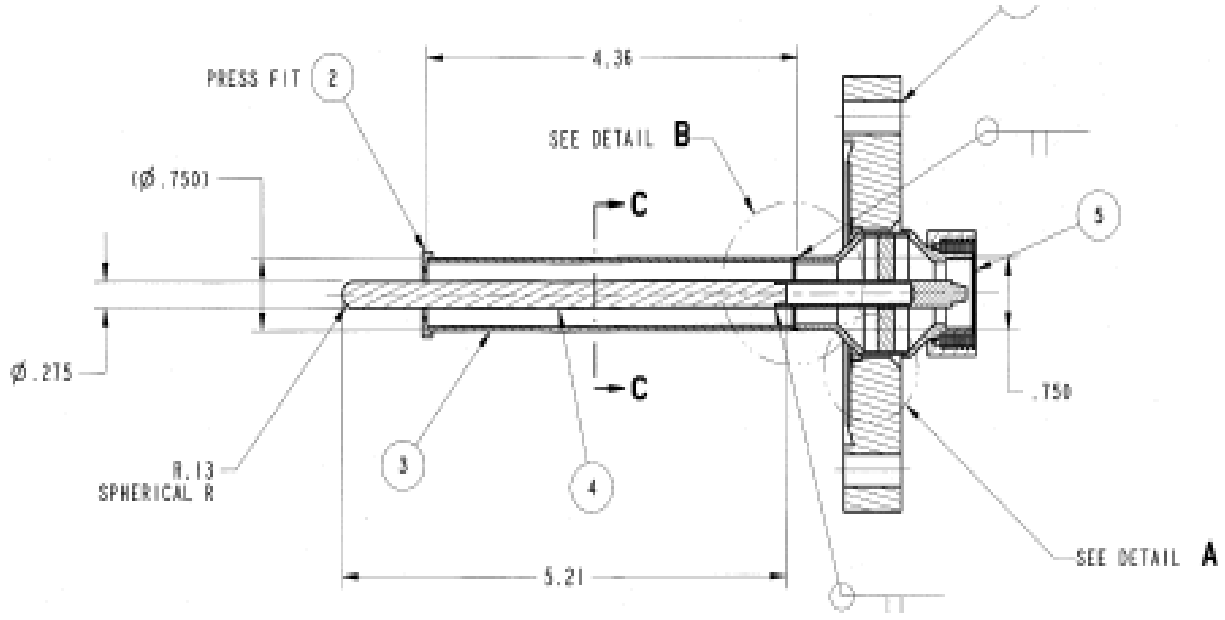

Figure 2.7 - Drawing of high-power coupler with dimensions

The feedthrough was mounted in a conflat-type flange and features a DIN 7/16 male connector. The coaxial conductors were welded to the vacuum side of the feedthrough. A schematic of the assembly is shown in Figure 2.7.

The coupler itself was designed to move inside a flexible bellows assembly bolted to the cavity and driven by a shaft connected to a screw right-angle actuator and a motor outside of the cryostat mounted to the top plate. The motion of the coupler is implemented through an isosceles linkage (also known as a Scott-Russell linkage) that translates vertical drive motion into horizontal motion perpendicular to the drive. In this implementation, the vertical load of the motor is reacted completely by the vertical mounting rods for the cavity and all horizontal loads are internal to the cavity and the coupler with no net horizontal loads experienced by the mounting rods. Thus, the position of the cavity is unaffected by the movement of the coupler. A schematic of the assembly appears in Figure 2.8 and a cutaway view of the coupler inside the cavity in Figure 2.9.

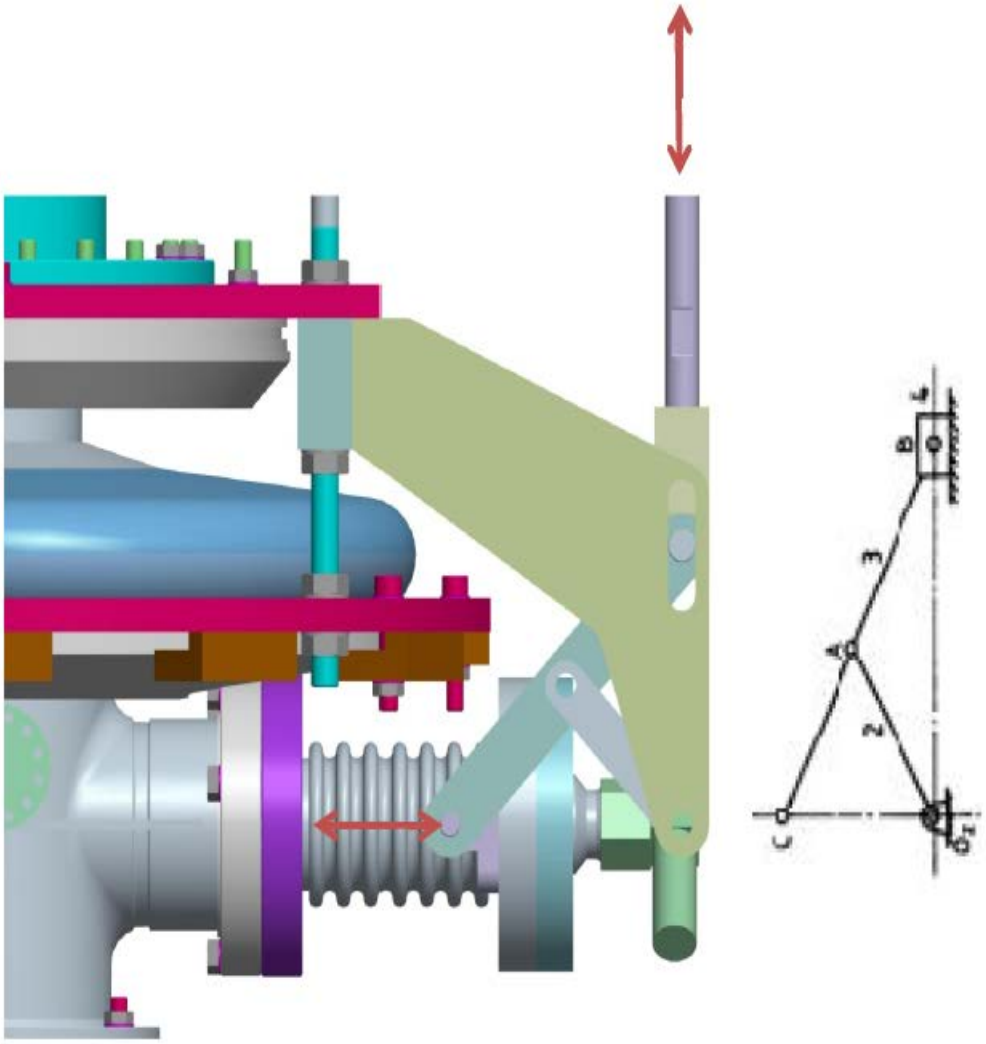

Figure 2.8 - Schematic showing the power coupler assembly at the cavity. The arrows show the direction of motion of the drive shaft and the bellows showing that vertical deflections translate the coupler horizontally into and out of the cavity, whose position remains fixed under translations of the power coupler. The inset at right shows the key features of the isosceles linkage.

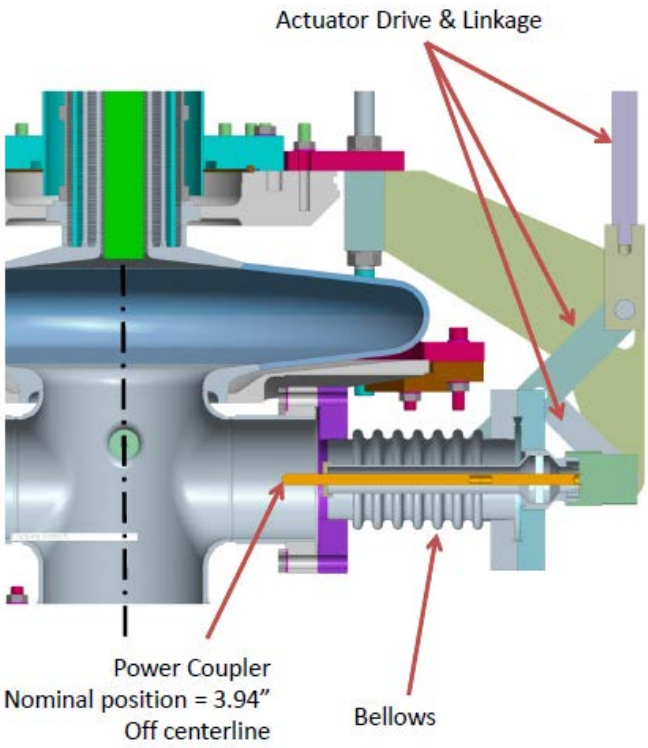

Figure 2.9 - Cutaway view of the power coupler inside the cavity showing the nominal position of the coupler when the bellows is relaxed.

Motion of the coupler is controlled by a stepper motor connected to a machine screw right-angle actuator and drive shaft that moves vertically. This allows for a maximum stroke at the coupler of ±15 mm. The maximum load at the cavity is 170 pounds, including friction, internal vacuum, the bellows at the cavity and at the top plate, and the weight of the drive shaft. There is no load at the bellows when it is at its relaxed length. The design incorporates rotating gears that have hard stops attached. These stops limit the motion of the motor at low torque as well as limit switches in both vertical directions of the drive that shut off the motor when the switches are actuated. In addition, a limit on current draw and duration of the motor constrains the force of the motor, stopping operation and engaging the brake when limits are exceeded. A linear potentiometer monitors the position of the drive shaft and is read by a digital controller that also reports the position of the stepper motor. The controller provides for several different modes of operation, allowing the user to specify the number of steps desired as well as the speed of motion. A schematic of the actuator and motor assembly on the top plate is shown in Figure 2.10. A schematic that shows the entire drive chain is shown in Figure 2.11.

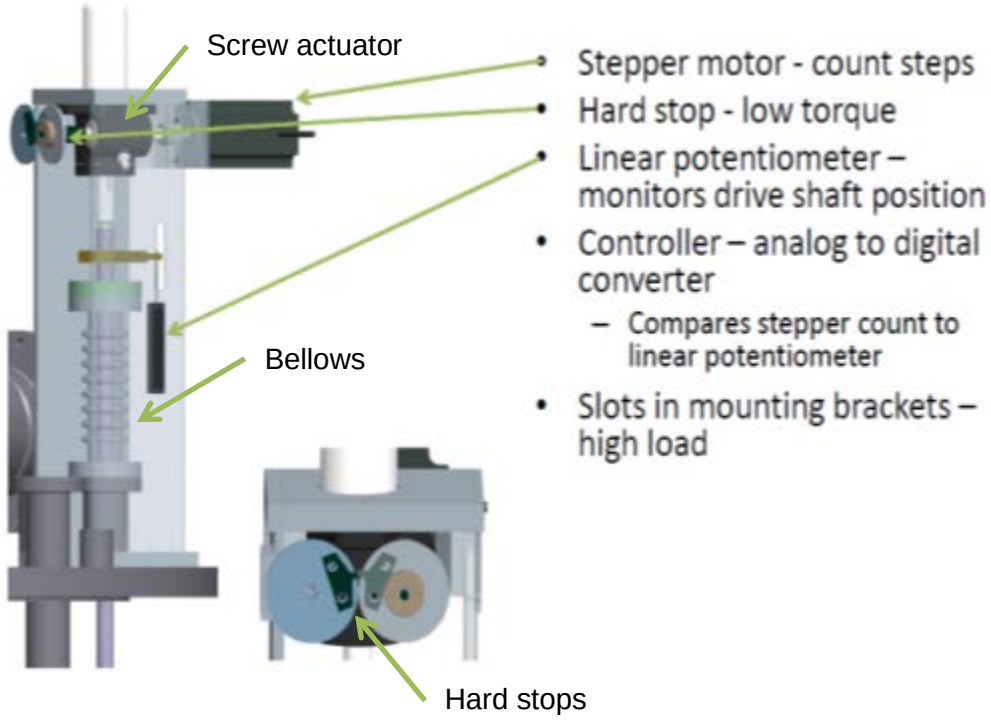

Figure 2.10 - Schematic of motor and actuator assembly. The motor and actuator assembly are mounted on the top plate, outside of the cryostat.

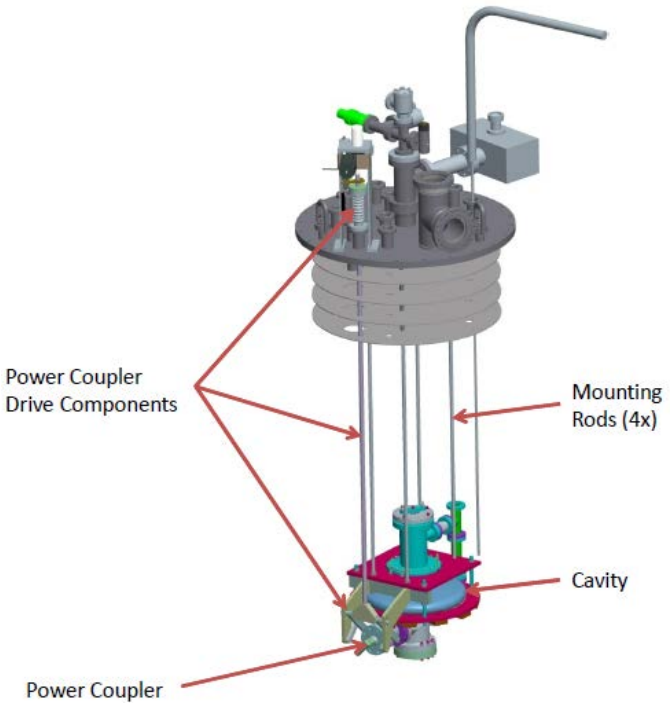

Figure 2.11 - Schematic of experimental assembly showing full drive assembly.

A subsequent modification of the design was implemented following the realization that the design did not properly constrain transverse deflections along the horizontal axis of the power coupler's motion. This situation would allow the coupler to roll about hinges attached to the bellows flange and allow the tip to move up and down inside the cavity. The situation is illustrated in Figure 2.12. For this reason, an alignment mechanism was added to the design that would, to some extent, constrain the motion of the coupler as it moved in and out of the cavity. The mechanism consisted of a rod moving inside a sleeve as shown in Figure 2.13. After some additional operating experience, the coupler motion was found to bind. As a result, the rod was undercut to allow more freedom of motion and prevent binding.

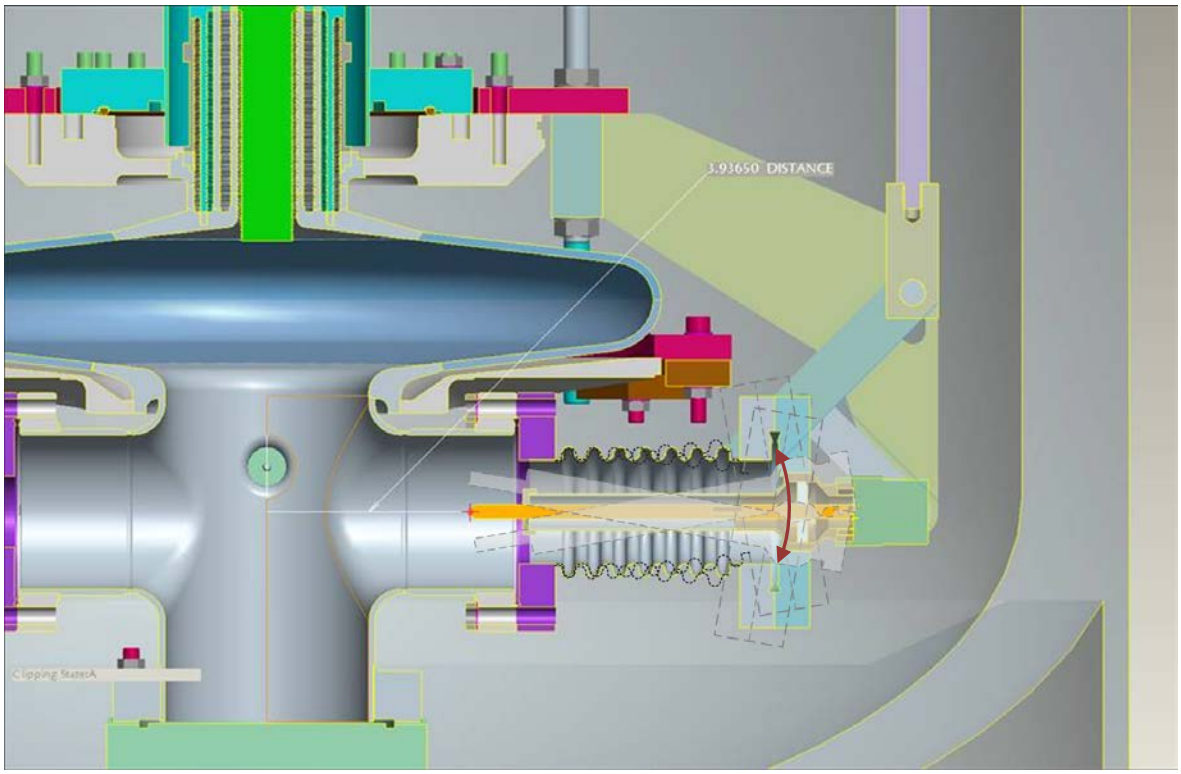

Figure 2.12 - Schematic of the coupler showing the (exaggerated) unconstrained transverse motion of the design. For this reason, an alignment mechanism was subsequently added to the design.

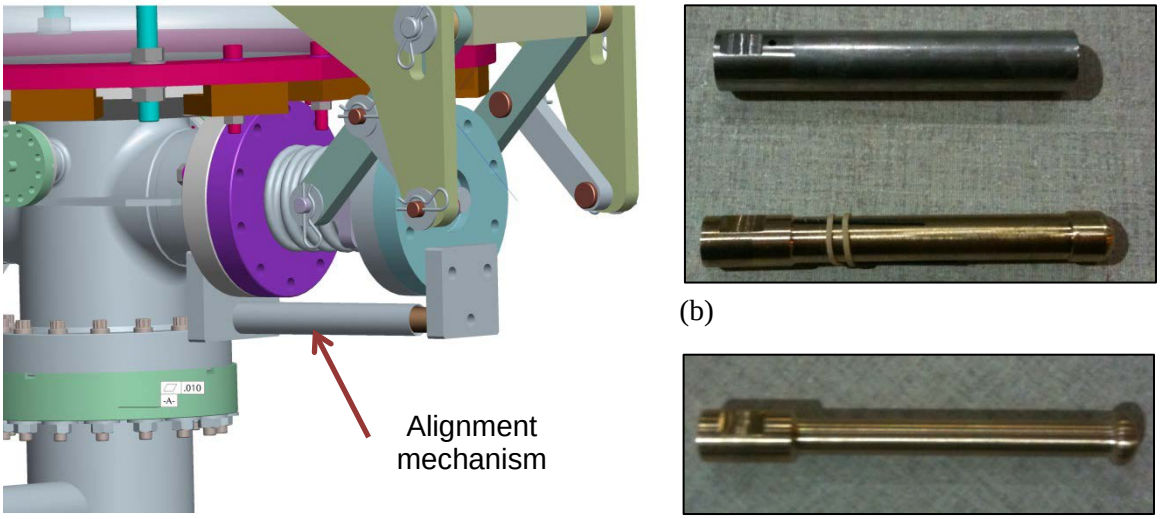

Figure 2.13 - (a) Schematic showing addition of an alignment mechanism to prevent transverse excursions of the coupler. (b) Photograph of the alignment sleeve (above) and rod (below) showing undercutting to prevent binding. Picture shows rubber band attached for measurement of radius during testing. (c) Modified rod with additional undercutting to further mitigate binding.

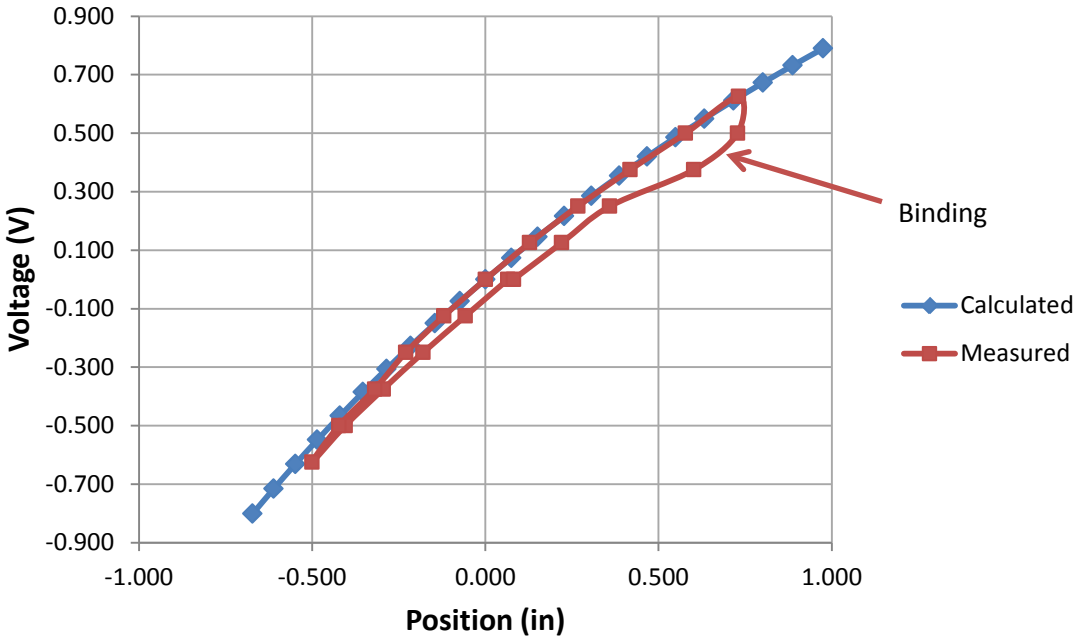

Figure 2.14 - Plot of normalized measured versus calculated coupler positions throughout range of motion of coupler. Zeros of both voltage and position are for the bellows at its relaxed length. Note that the measurement shows significant hysteresis. Also, near the upper right portion of the measurement there is indication of binding shown by the irregular path of the curve.

2.5 Magnetic Shielding

A layer of magnetic shielding was added to the outside of the dewar along with a shielding plate that was placed on top of the lowermost baffle inside the dewar. Schematics of the outer shielding assembly are shown in Figure 2.15 and Figure 2.16. A schematic showing the penetrations and dimensions of the inner baffle plate shielding insert is shown in Figure 2.17. The shielding was fabricated by Amuneal Fabrication Corporation. The thickness of all shielding pieces was 0.062 inches.

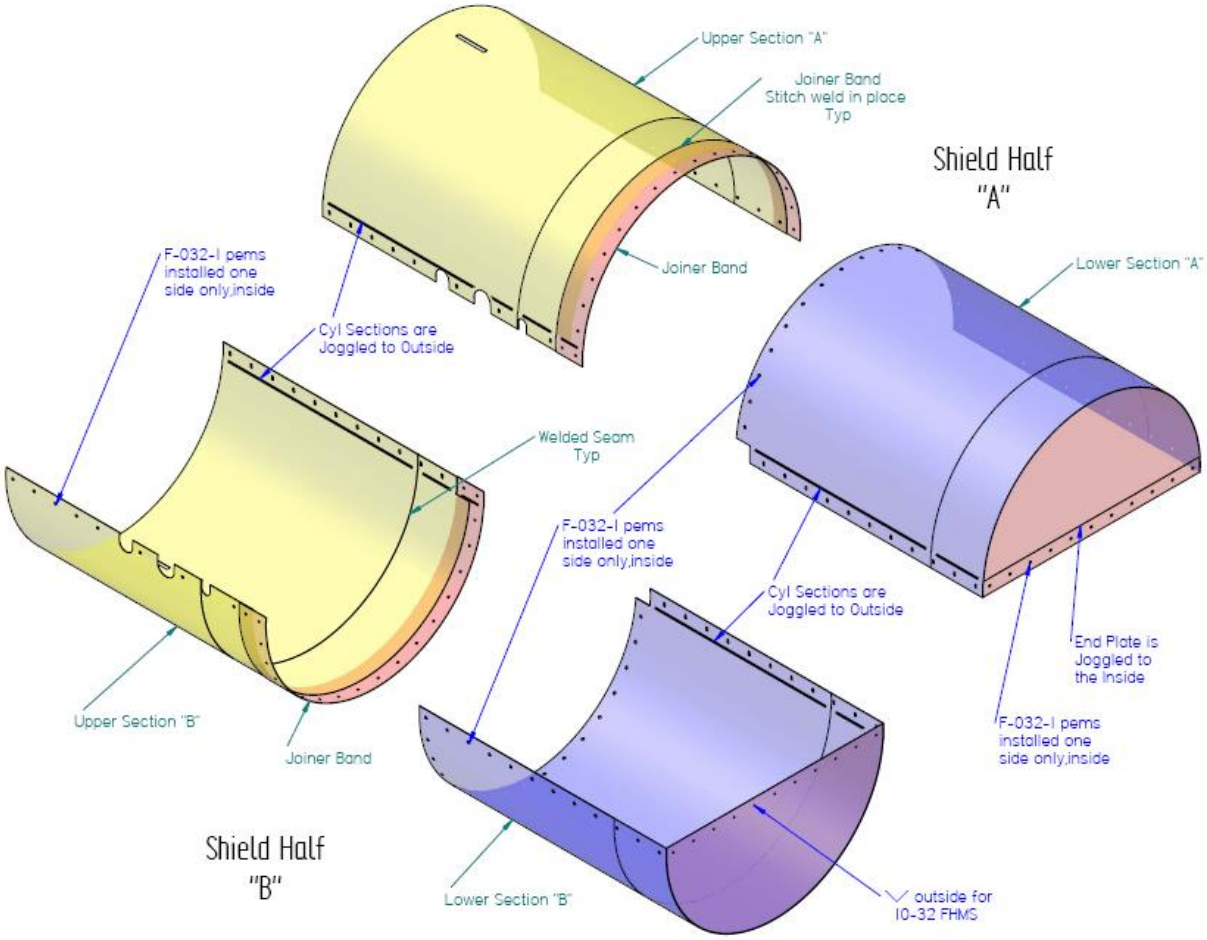

Figure 2.15 - Exploded view of the clamshell arrangement of the magnetic shielding.

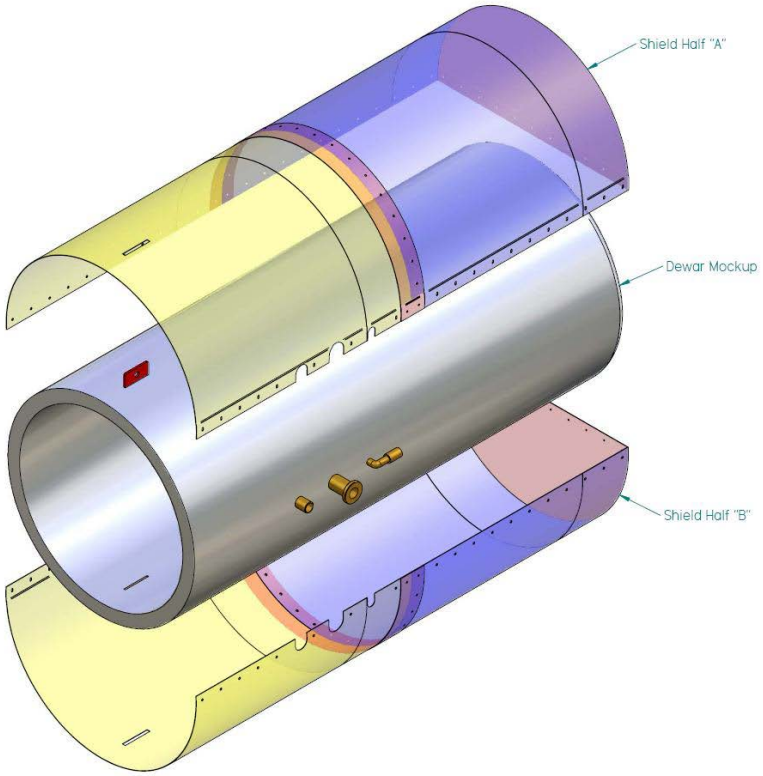

Figure 2.16 - Clamshell arrangement of magnetic shielding and placement around cryostat.

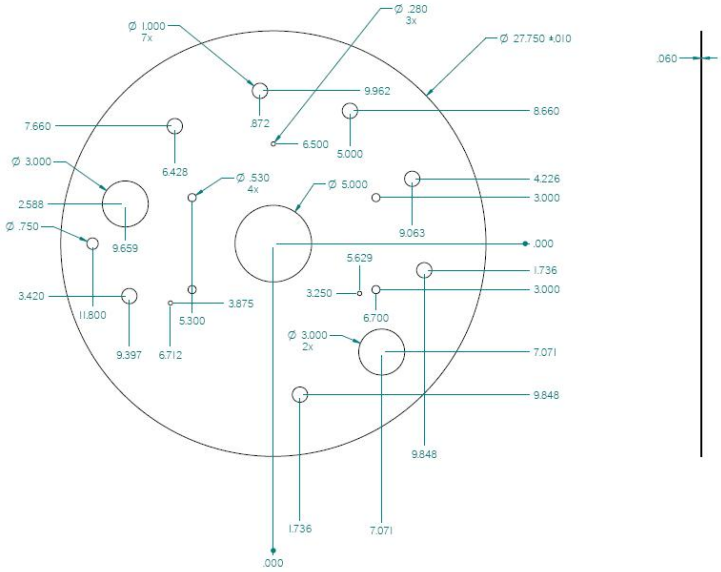

Figure 2.17 - Dimensions of baffle plate shield inserted inside dewar showing penetrations and thickness.

The expected attenuation of the shielding was a factor of 29 based on the catalog values provided by Amuneal. Measurements of the actual attenuation were performed with the assistance of J. Muratore from the Superconducting Magnetic Division. Both transverse and axial (vertical) measurements of the magnetic field were made both outside the dewar, to establish the ambient magnetic field, and inside the dewar to establish the extent of the shielding. For the inside measurement, the inner shield plate was in place along with the top plate, and the field was sampled at various depths from the top plate including the depth of the center of the suspended cavity, 1.45 m from the bottom of the top plate and through various ports. The locations of these ports are shown in Figure 2.18. Note that the picture shows the unmodified top plate before a port was added for the drive mechanism of the power coupler. The measurements were made before the top plate was modified to include the extra port. The measurements of the outside of the dewar are shown in Figure 2.19 and indicate an averaged ambient field of between ~23 and ~25 mT at the center of the dewar without shielding.

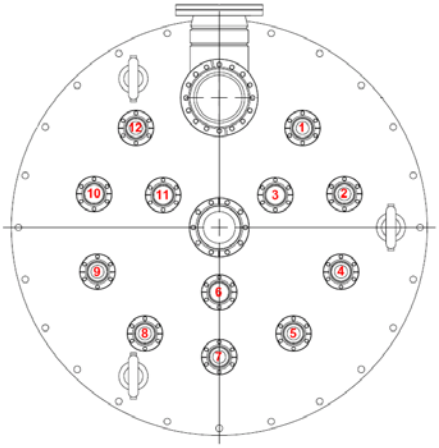

Figure 2.18 – Top plate showing numbering scheme for port identification during magnetic measurements.

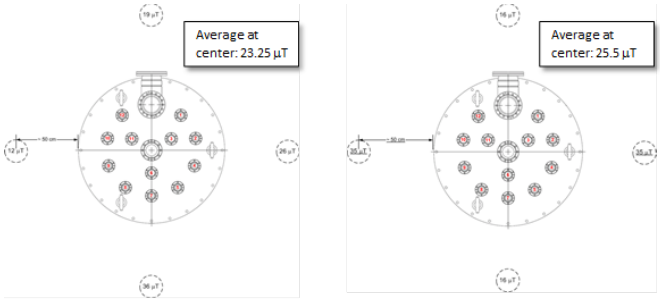

Figure 2.19 - Measurement around exterior of cryostat to determine ambient magnetic field.

The measurements inside the dewar are shown in Figure 2.20 and Figure 2.21 for several different depths and at various ports. The axial measurements indicate that the field at the cavity center (the second diamond from the right in each plot) is a factor of ~53 less than the averaged outside field at the center and a factor of 69 less than the field measured at the top. Comparable results are obtained for the outer ports. Transverse measurements show that at the cavity center, the attenuation factor is ~2,550 at the cavity center and ~212.5 at an outer port considering the averaged outside field. These measurements appear to be much better than the expected attenuation of 29 that were calculated. Presumably, the calculated attenuation is the expected change in flux density at the immediate inner and outer surfaces of the shielding. These measurements are performed at various distances away from these surfaces.

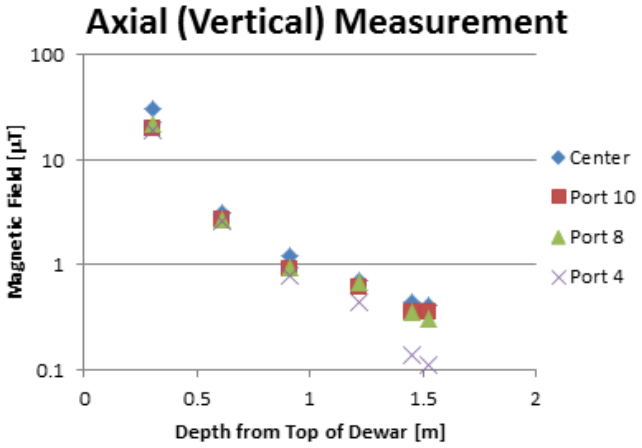

Figure 2.20 - Axial magnetic field measurements at various port locations as a function of distance between probe and bottom of top plate.

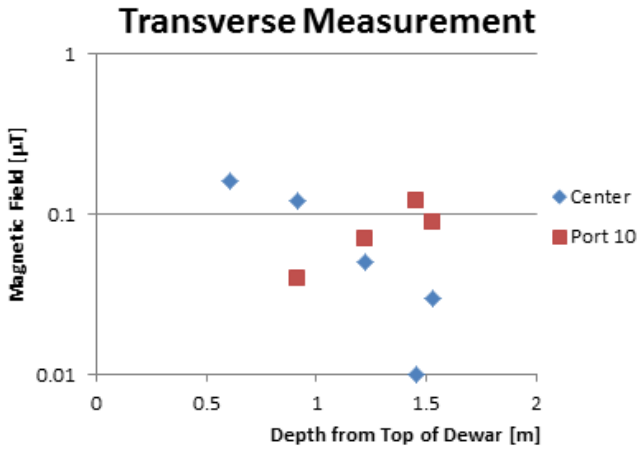

Figure 2.21 - Transverse magnetic field measurements at two different port locations as a function of distance between the probe and the bottom of the top plate.

2.6 Cavity and Dewar System

The cavity must be submerged in a liquid helium bath and its temperature reduced to at least 4.2 K in order for the cavity to become superconducting. Therefore, the cavity was suspended from four threaded rods attached to the top plate of a 28" dewar. A schematic of the entire assembly is shown in Figure 2.22 and dimensions for the assembly are given in Figure 2.23. In addition, Figure 2.24 shows a photograph of the assembly during the early stages of experiment construction.

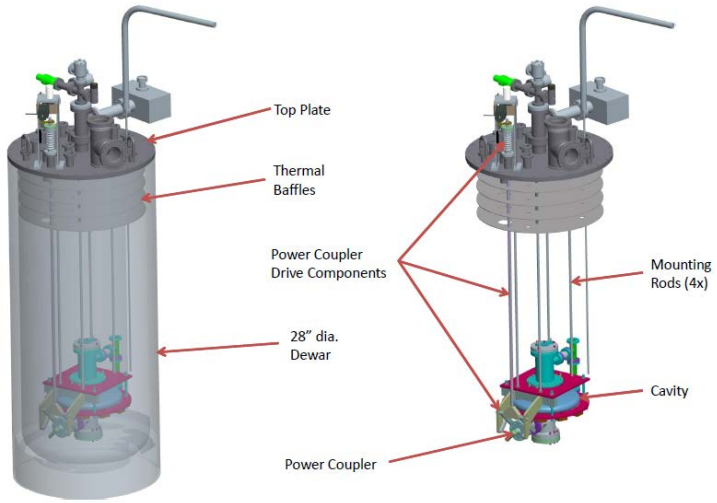

Figure 2.22 - Schematic of cavity and dewar assembly.

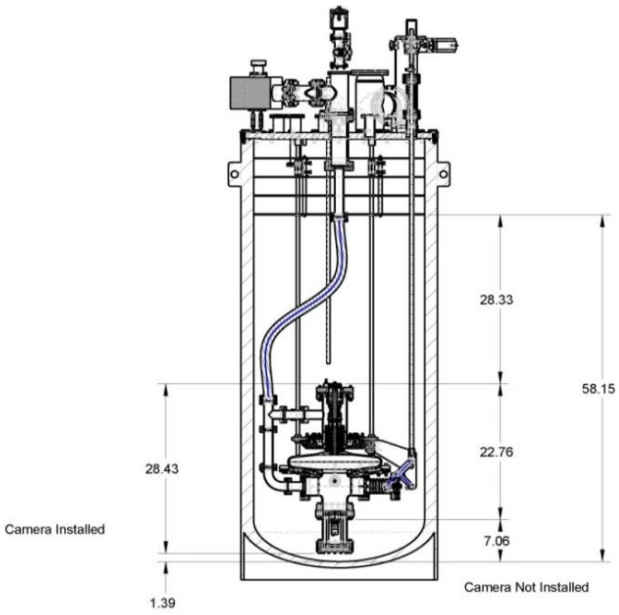

Figure 2.23 - Cavity and dewar assembly with dimensions shown. Note that the camera chamber is shown in the schematic, attached to the bottom of the cavity.

Figure 2.24 - Photograph of the cavity attached to the top plate during initial test preparations. The top plate rests on a support frame, and the cavity is suspended from the top plate by support rods that pass through the four baffle plates. In addition, a flexible vacuum hose, not shown in the picture, attaches to the cavity and passes through the baffles.

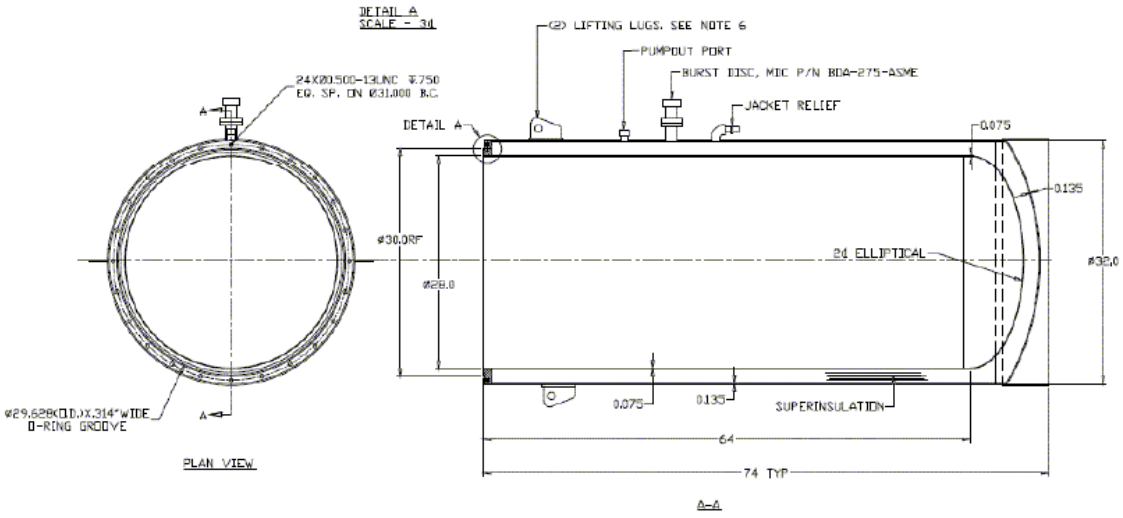

Figure 2.25 - Schematic of 28" dewar used for Large Grain test.

The dewar was manufactured by Cryofab, Inc. and was designed to meet the ASME 2007 Boiler and Pressure Vessel codes (MAWP = 37 psi) and was reviewed in the Laboratory Experimental Safety and Health Committee (LESHC) minutes of October 14, 2011. The dewar is vacuum insulated and operates at slightly above 1 atm absolute pressure. The dewar is filled and its level maintained from a local liquid helium storage dewar via an external fill valve. Furthermore, the dewar is fitted with a removable top plate and baffle plates that allow for the setup of various experiments. In addition, the dewar include pressure relief ports for both the insulating jacket as well as the interior of the dewar. A schematic of the dewar appears in Figure 2.25.

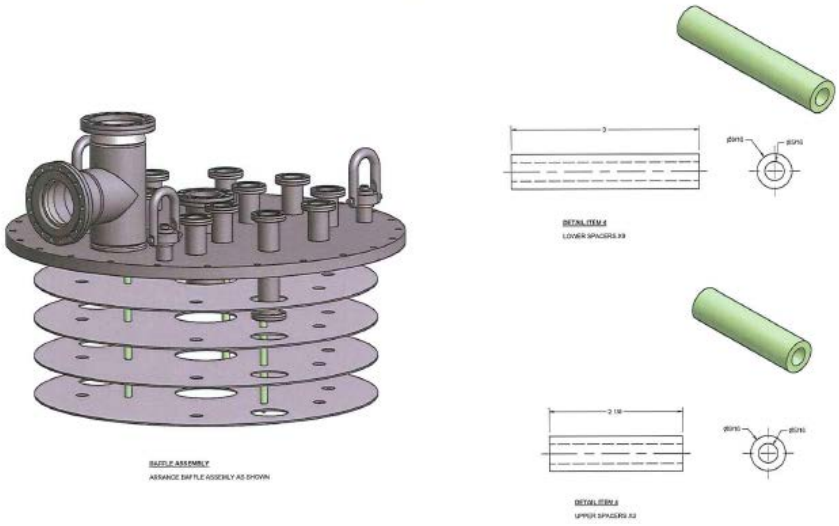

Figure 2.26 - Top plate and baffle assembly for the 28" dewar. The baffle spacers, made of G10 material are also shown. Note that the schematic shows the original design of the top plate before modifications.

The top plate of the dewar is also designed to meet the requirements of the ASME 2007 Boiler and Pressure Vessel code and was manufactured by PHPK along with the baffle plates. Modifications to the top plate were introduced to the original design to accommodate the supports of the cavity including the addition of a single 2 ¾" half-nipple penetration for the power coupler actuator shaft. The modifications maintained compliance with the ASME standard and were completed by the manufacturer. Figure 2.26 shows the top plate and baffle assembly.

Four baffle plates rest on retaining pins that are connected to mounting shafts directly under the plate. The plates were modified by adding additional holes to allow clearance for mounting rods and the actuator shaft.

2.7 Vacuum System

When the experiment is fully assembled, the vacuum system is comprised of two separate volumes that require evacuation: the RF cavity and the camera chamber. The vacuum system required to achieve superconducting helium temperatures is a part of the cryogenic system and is not discussed in detail in this report. The schematics of the vacuum configuration are shown in Figure 2.27. The RF cavity is under ultra-high vacuum with pressures of 10^{-8} Torr or lower achieved using a combination of turbo pump for roughing and ion-pump for maintenance of UHV while the camera chamber is under insulating vacuum pressure of < 10^{-3} Torr. Calculation of required pressure relief for each volume was performed and is detailed in the report of the engineering analysis of R. Than documented in the Laboratory Environment Safety and Health Pressure and Cryogenic Safety Subcommittee (LESHC-PCSS) review of November 2010. The two volumes are separated by a sapphire viewport that allows the camera to view the interior of the cavity.

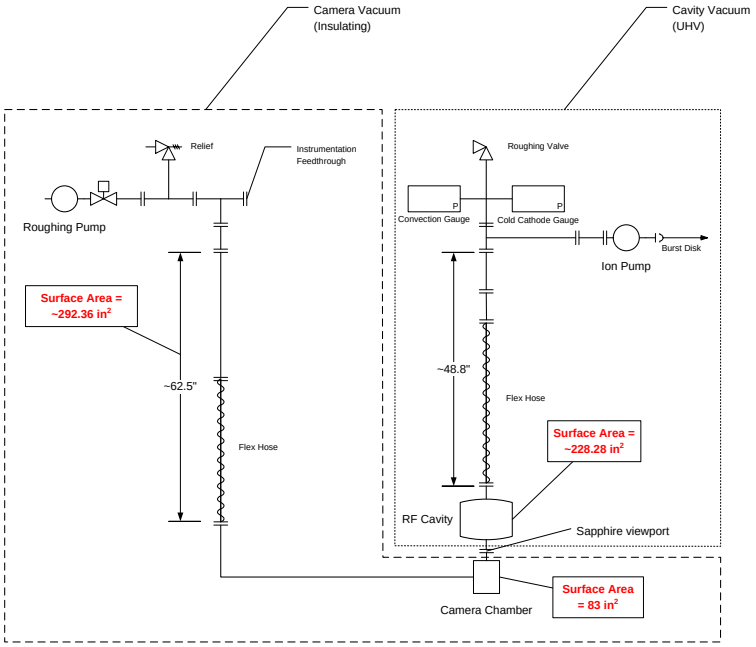

Figure 2.27 - Schematic instrumentation diagram showing vacuum components of cryostat.

2.8 Cooling

The cavity is cooled by transferring liquid helium from a storage dewar into the cryostat located in the SVTF. The transfer rate is controlled by the pressure on the storage dewar and the diameter of the transfer line which is fairly narrow, requiring long transfer times, as described later in the report. The rate of transfer was monitored by inspection of the various temperature probes arrayed around the cavity in the cryostat and by a level probe measuring the level of liquid helium in the cryostat. Since the level probe did not reach all the way to the bottom of the cryostat, liquid levels could only be registered after liquid had collected in the cryostat for some significant length of time after transfer of the cryogen had commenced, usually after many hours. Temperature monitors turned out to be the most important measure of early cooling efforts, since location and reading on the monitors was directly correlated to the liquid level inside the cryostat. A diagram showing the positions of the various temperature sensors is given in Figure 2.28.

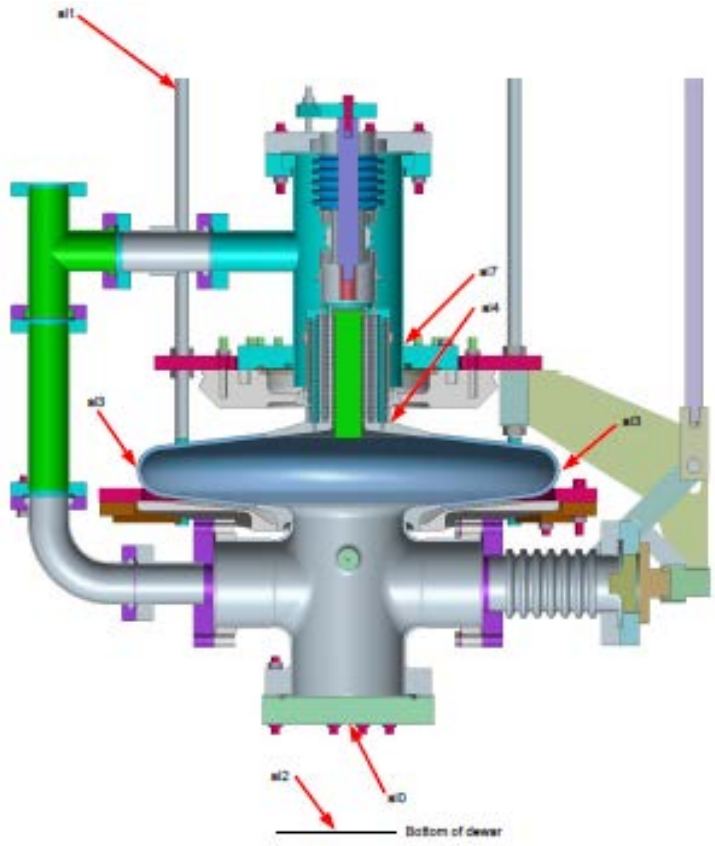

Figure 2.28 - Position of temperature sensors in the experiment. The arrows point to the position of the sensors. Note that one of the sensors is located at the very bottom of the cryostat and, when the camera chamber is attached, the sensor ai0 is the attached to the outside of the camera chamber.

Both 2 K and 4 K performance were measured, and temperature inside the cryostat was controlled by regulating the pressure inside the cryostat. The cryogenic system allowed the pressure to be maintain from atmospheric down to subatmospheric pressure as required to achieve 2 K temperature.

2.9 RF System

The RF system for the large-grain cavity consisted of two basic subsystems that were each used separately along with a power-meter interface unit that was used for routing power to and from the cavity to a power meter for measurement. A phase-locked loop system was initially employed for exciting the cavity, and, later, a self-excited loop system was added. Each of these subsystems is briefly described below.

2.9.1 Phase-Lock Loop

The RF hardware was originally designed by C. Schultheiss around a phase-locked loop system that had first been used in the ERL for testing of the give-cell LINAC cavity. In the ERL version, digital control of the phase shifter, tuner, and magnitude attenuation had been included in the design, but these features were removed for use in the large-grain system. For the large-grain system, analog control of the phase shifter and frequency offset (included as part of the baseband signal conditioning system) was included through use of adjustable voltage supplies. The design also features interlock circuitry for inhibiting the RF power, but this feature was not used in the experiment, and the switch circuitry was bypassed. It should also be noted that the Pulsar phase shifter was eventually replaced by a manual phase shifter. A schematic of the system appears below in Figure 2.29.

2.9.2 Self-Excited Loop

The self-excited loop system was added to the low-level RF as a means of simplifying the excitation of the cavity and verifying the resonance frequency. The decision was driven by concerns raised in the first test about the difficulty encountered in stimulating the cavity, and it was envisioned that the experiment could readily switch between the phase-locked loop system and the self-excited loop as desired. C. Schultheiss once again designed the system in a manner that could be added to the existing RF system with minimal disruption. As testing of the SEL system progressed, amplification of the signal transmitted from the cavity was added to the relatively weak coupling ($Q_{ext} \sim 10^{11}$) of the pickup probe to the cavity. A block schematic diagram of the system appears in Figure 2.30. As in the case of the phase-locked loop, the Pulsar phase shifter was eventually replaced with a manual phase shifter.

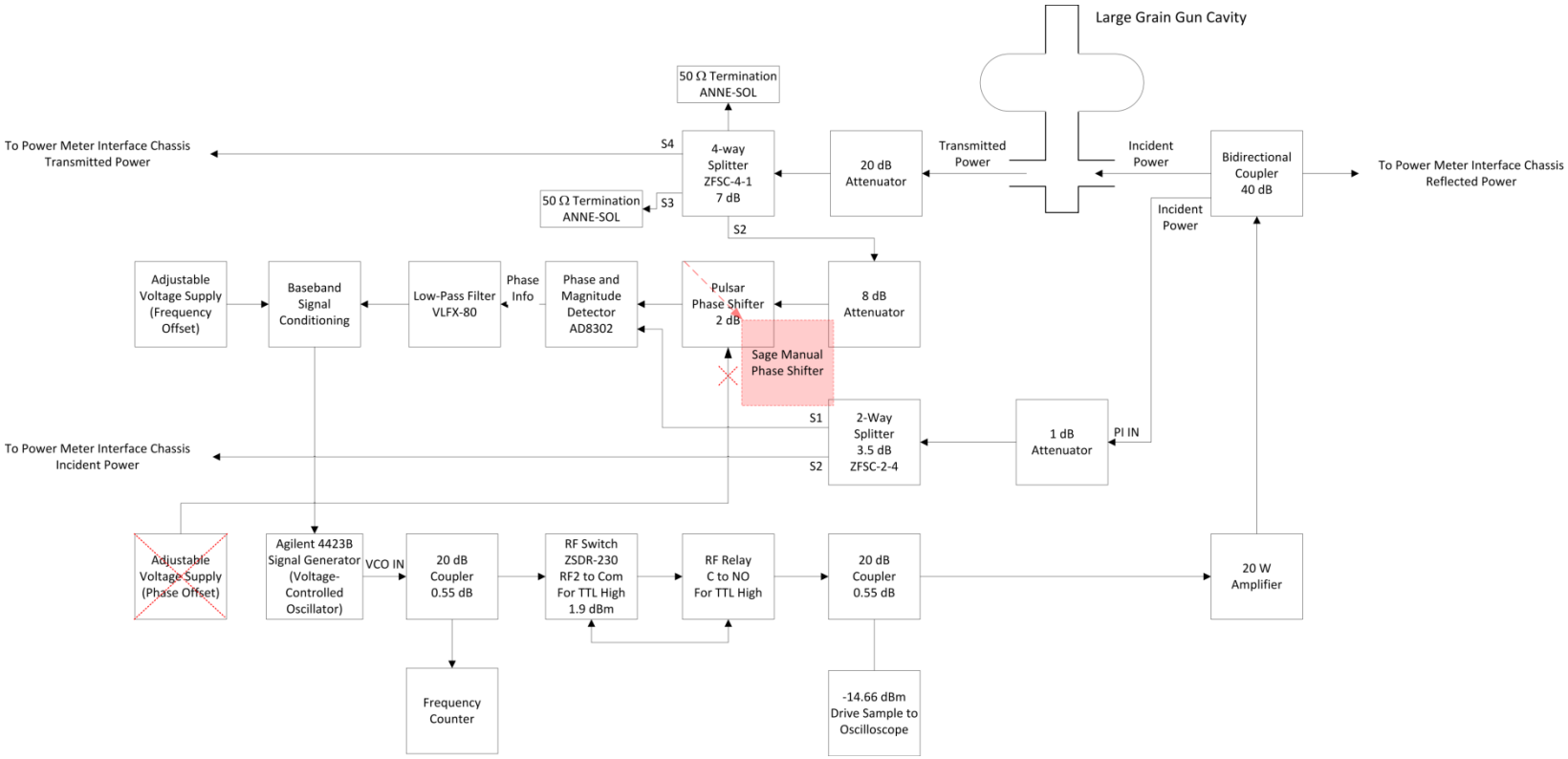

Figure 2.29 - Phase-locked loop system for the large-grain gun. The replacement of the Pulsar phase shifter by the manual phase shifter is noted by the red, dotted square block.

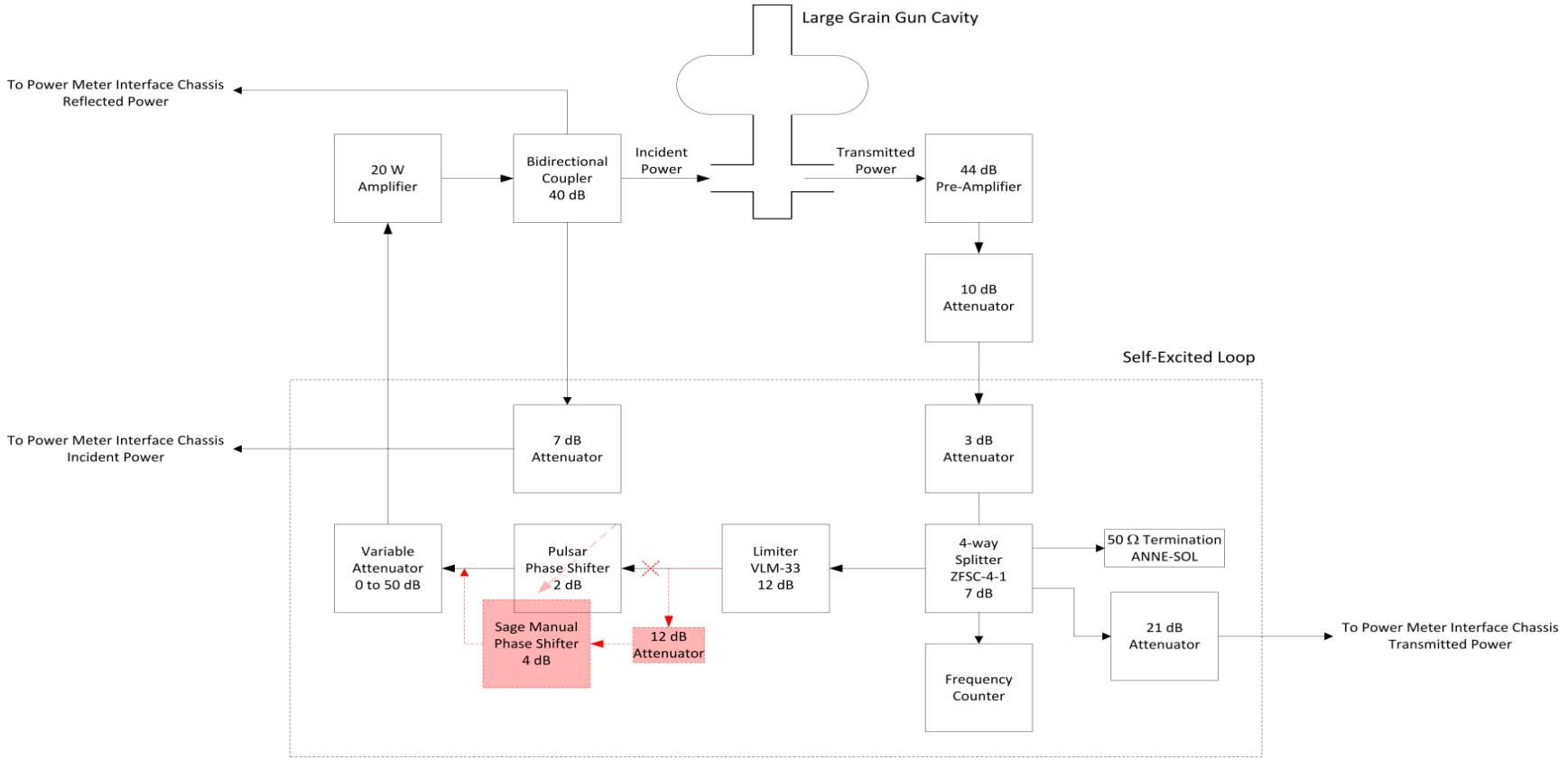

Figure 2.30 – Block schematic diagram of the self-excited loop for the large-grain RF system. Note the replacement of the Pulsar phase shifter with the manual phase shifter and the addition of a pre-amplifier to the transmitted signal of

2.10 Camera and Chamber

A camera has been included in the large-grain project to detect signs of multipacting in the vicinity of the choke joint and to assist with pinpointing its exact location. Initially, design plans called for the camera to be located outside of the cryostat chamber and to use a series of appropriately placed mirrors and a viewport attached to the cavity in order to view the interior of the cavity. However, after considering the design of an experiment to explore unrelated luminous phenomena in cavities [7], a modification to the design was implemented that would place the camera into the cryostat and attach it directly to the cavity to view the interior of the cavity through a sapphire viewport. The design considerations and features are provided in the following sections.

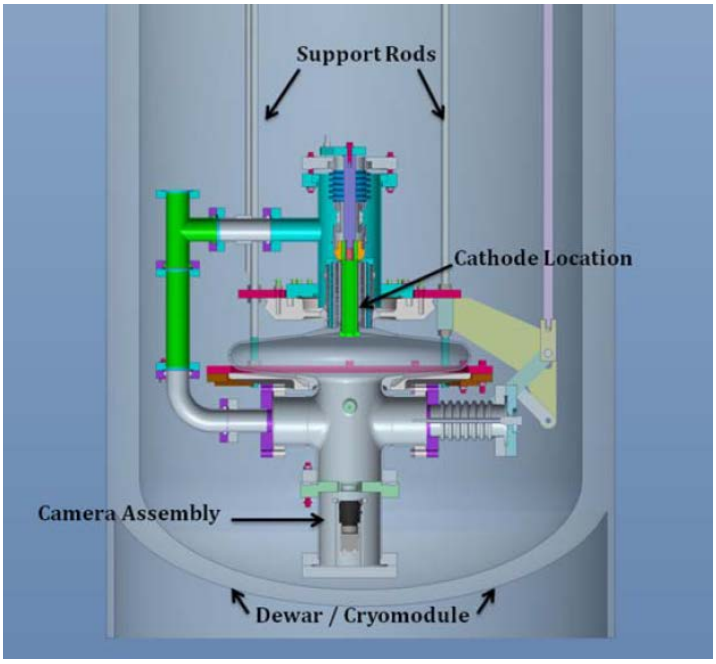

Figure 2.31 - Schematic of experimental assembly with camera chamber installed.

2.10.1 Camera

The camera selected for the project was the Flea 2 CCD camera manufactured by Point Grey. Calculations performed by S. Bellavia showed that the 40 mm diameter optical target presented by the choke joint would just fit onto the 1/2" CCD chip provided by the camera, providing a maximum resolution of about 10 microns. See Figure 2.31 for a schematic view of the layout. Since the aim of the camera is to image the multipacting that may be taking place in the choke joint of the cavity, we

also sought a CCD element that is sensitive in the visible-to-UV range of the electromagnetic spectrum which we believe to be the most likely range of wavelengths for resonant emissions. The Flea 2 camera is an inexpensive option that features a Sony ICX267 CCD sensor whose sensitivity was deemed adequate in the near-ultraviolet range for initial stages of testing. The response curve for the sensor is shown in Figure 2.32. The success of imaging at the camera also depends critically on the choice of viewport material since light must pass through the viewport to reach the camera. For this reason, a sapphire viewport was also chosen. The spectral curve of sapphire is included in Figure 2.33. The camera supports a maximum resolution of 1392 × 1032 pixels with a pixel size of 4.65 × 4.65 µm. A photograph of the camera along with a schematic is shown in Figure 2.34. A ThorLabs MVL35M23 was purchased for use with the camera. The lens is a 35 mm, f/2.0, C-mount threaded lens and includes a thumbscrew to lock the aperture and focus of the lens (see Figure 2.35).

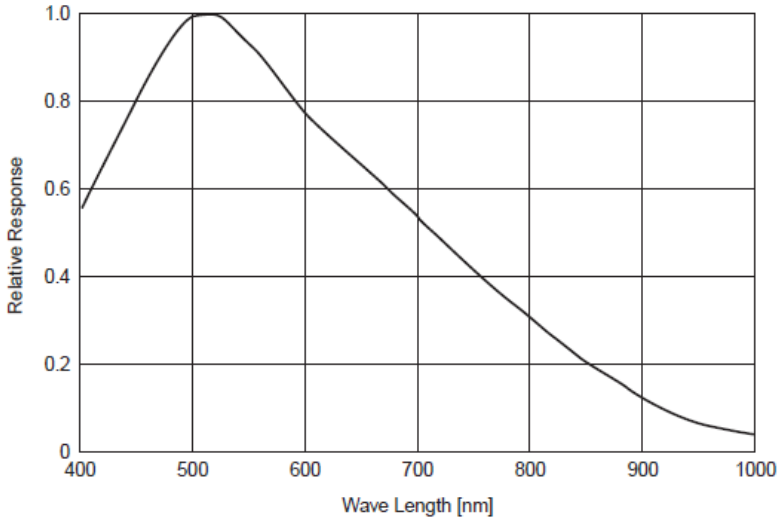

Figure 2.32 - Spectral response of Sony ICX267 CCD. In order to view multipacting, the aim was to maintain sensitivity in the near-UV range around 400 nm.

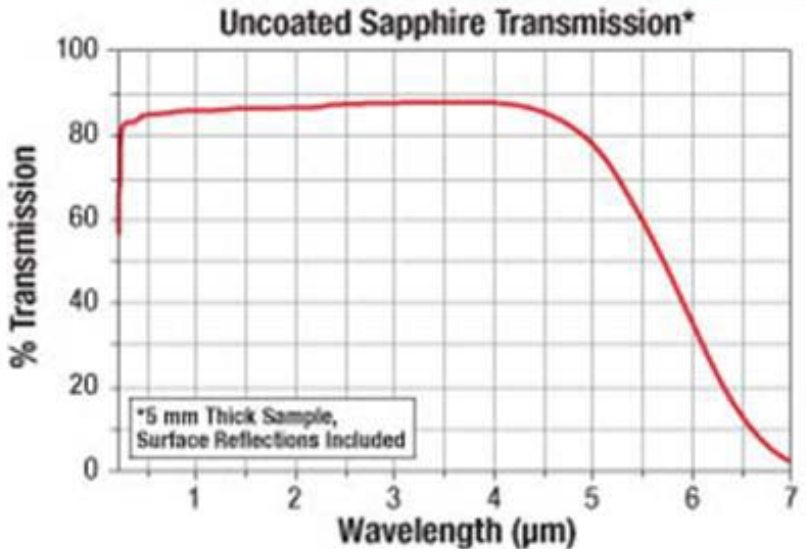

Figure 2.33 - Sapphire transmission response. Note the relative transparency in the range below 500 nm.

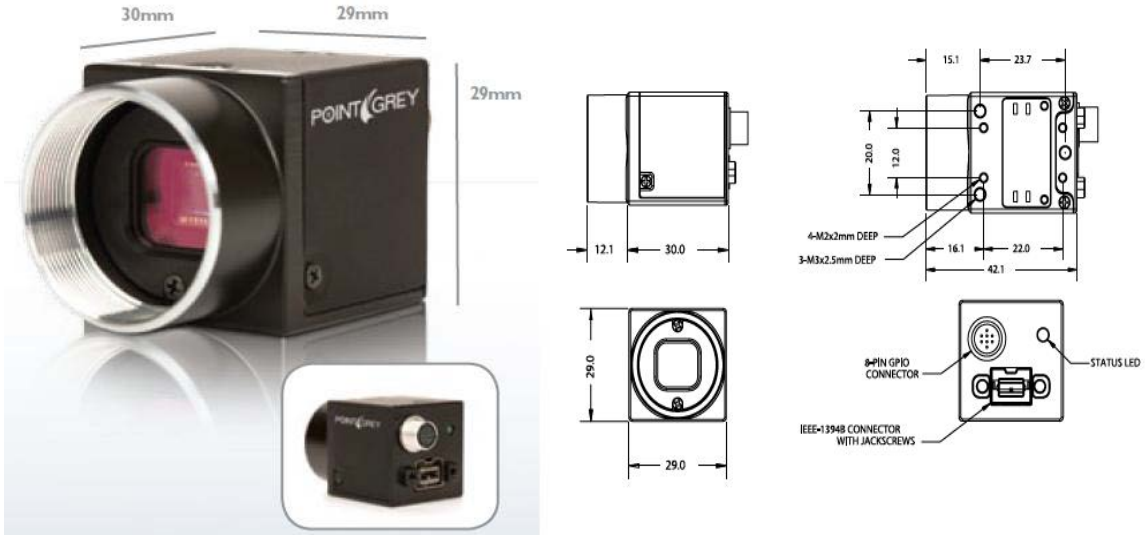

Figure 2.34 - The Flea 2 Camera.

Figure 2.35 - Flea 2 camera along with ThorLabs MVL35M23 lens. Note that the cover of the camera body has been removed in order to aid in evacuation of the camera chamber and prevention of trapped volumes.

In addition, the camera features an IEEE-1394b ("Firewire") interface for transmitting data. This interface was used in combination with 1394-to-Coax dongle (EQCO-FW5001) manufactured by EqcoLogic to transmit the data from the camera over a shielded coaxial cable to a vacuum feed-through on the top plate of the cryostat for downstream delivery to a laptop computer. Because the coaxial cable inside the cryostat runs through the vacuum tubing used to evacuate the camera chamber, a special procurement of cable with the outer jacket removed was obtained from Advanced Technical Materials (CF100-120-SM-SM/BNL) with an outer diameter of 0.110 inches.

An important advantage of using the Flea 2 camera was that Point Grey offers a software package that can be used to easily control the camera as well as manage and save image. The software allows various operating modes of the camera to be selected that change the image size and frame

rate of the camera among other parameters. It was found, however, that the use of the dongle restricted the camera to 15 fps with an image size of 640 × 480 pixels. However, this restriction was found to be adequate to obtain suitable images from the camera for initial testing. This software was also used to control a rudimentary lighting system consisting of four LEDs that were attached to the camera to provide lighting of the interior of the cavity for initial testing since no other source of light would be present. A simple circuit was constructed that would allow the lights to flash or remain on steadily in response to software controls with power for the lights derived from the camera itself.

Several important questions were addressed during testing of the camera to make sure that they could be adequately managed including heating and outgassing of the camera during operation. Heating would be of particular concern during operation since the camera would reside in a chamber under insulating vacuum, preventing dissipation of camera heat through convection. Furthermore, conduction of heat from the camera to the surrounding chamber would be limited by design (see the discussion of the chamber below). Outgassing was also a concern due to the necessity to maintain insulating vacuum in the camera chamber while immersed in the helium bath both to prevent heat transfer to the bath and to prevent formation of frost on the camera lens and imaging system.

To test the heating of the camera, the camera was operated for a prolonged period (~ 3 hours) while mounted in the camera chamber. The chamber was pumped down to insulating vacuum pressure and both the temperature of the camera and the pressure inside the chamber were measured while the camera was delivering image data to determine the temperature profile and the outgassing rate of the camera. The temperature of the camera was found to plateau around 45-degrees Celsius and the outgassing rate is given below in Figure 2.36. The temperature data was reassuring in that no runaway condition was observed. At the same time, image quality was maintained throughout the test and no data delivery errors were observed.

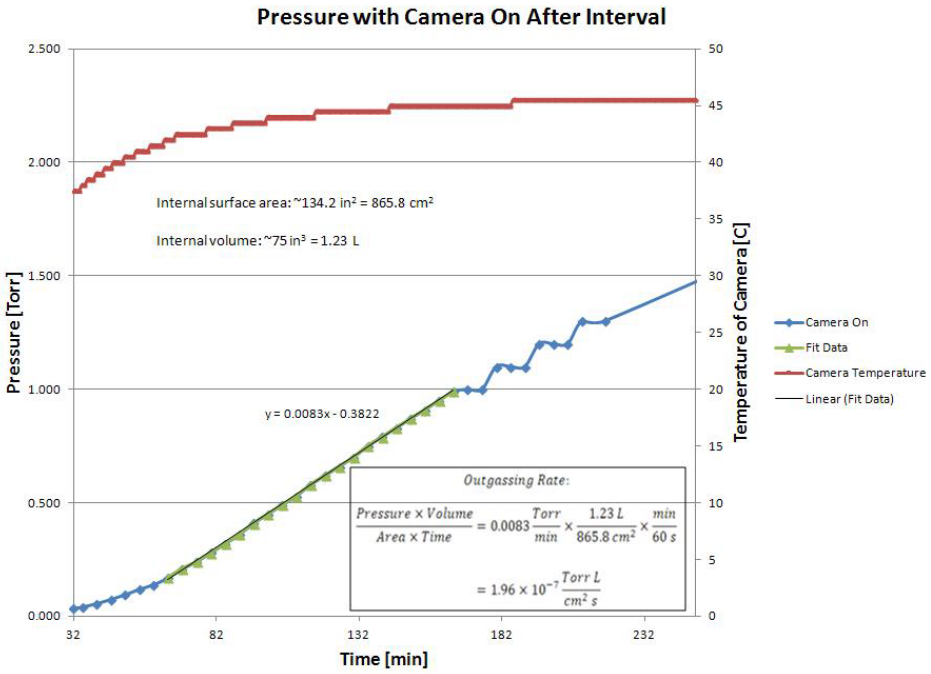

Figure 2.36 – Study of the pressure and temperature of the camera in the chamber showing the rise in temperature and pressure (without pumping) indicating the outgassing rate of the camera.

It was deemed likely that cryopumping would be sufficient to control the pressure after immersion of the camera chamber in the helium bath. It was also deemed likely that frosting would not pose a significant issue due to the significant cryopumping that could be expected. These suppositions would be confirmed during initial testing of the camera as discussed later in the report. To optimize vacuum pumping and prevent trapped volumes within the camera, the outer metal case of the camera was removed when the camera was installed.

2.10.2 Camera Chamber

The camera chamber and camera mounting scheme was designed by S. Tuozzolo and C. Cullen. The details of the design are detailed in S. Tuozzolo's design report [8]. To summarize the essential features, the design was conceived to contain the camera and be attached to the large-grain RF cavity. The chamber height was required to be kept to a minimum in order to allow the cavity to be submerged as deeply as possible into the helium bath. Furthermore, the camera requires an unobstructed view of the interior of the cavity, requiring a sapphire viewport.

To meet these requirements, the camera was mounted inside a cylindrical section of steel attached to the bottom of the existing gun assembly with a custom flange using a hex seal. The camera is ori-

ented to face up directly into the RF cathode and cathode choke joint through a 1" diameter sapphire window welded into the flange of the chamber. The camera is mounted using G10 fiberglass rods for support and to minimize heat conduction from the camera. ANSYS simulations were performed to confirm the thermal conduction properties of the setup. While there were initial concerns about the camera losing too much heat and becoming too cold, it was quickly realized during the course of testing that the camera would be a significant heat source and testing was conducted as described above to insure that the camera operate properly in the evacuated and insulated environment of the chamber. A schematic of the chamber is shown in Figure 2.37. The chamber is evacuated using a turbo pump, and the vacuum system is completely separate from the cavity vacuum as outlined in the section on the vacuum system.

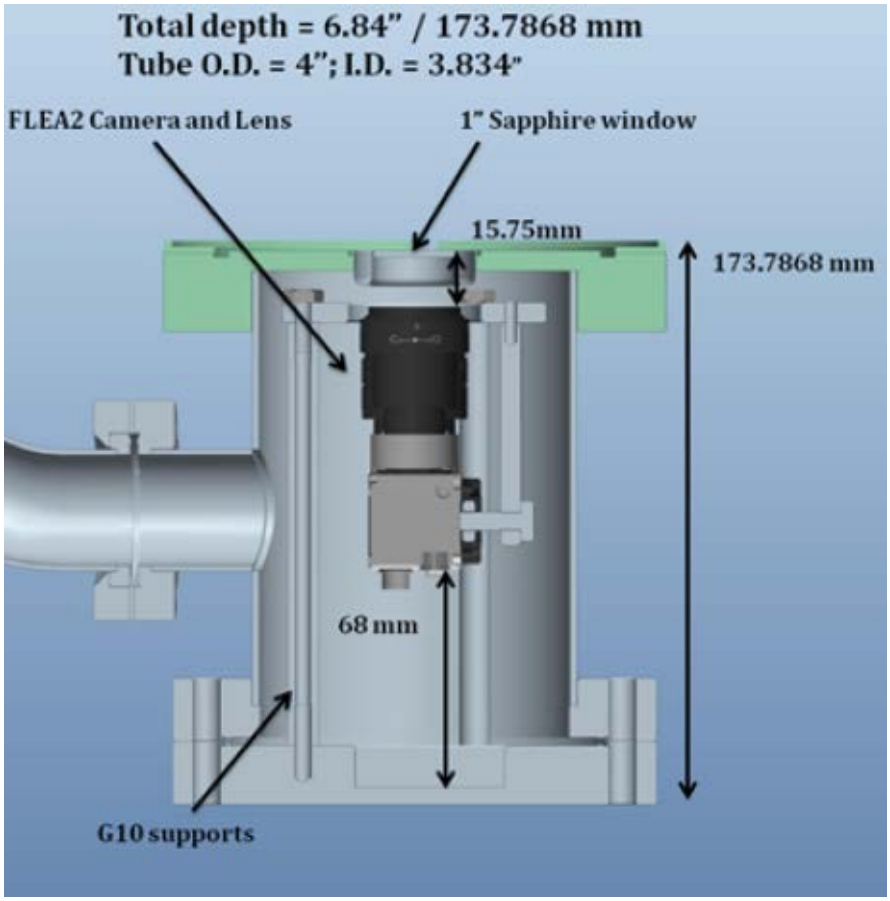

Figure 2.37 - Schematic of camera chamber.

2.11 Experimental Safety Considerations

Extensive safety reviews of the experiment were carried out that are detailed in other documents, and they are referenced here for the sake of completeness. Much of the safety review of the Small Vertical Test Facility and the 28" Test Dewar is documented in the Laboratory Environment Safety and Health Pressure and Cryogenic Safety Subcommittee (LESHC-PCSS) review of November 2010. This review addresses the ODH considerations of the facility, hazard identification, standard operating procedures for transfer of helium, pressure relief calculations, pipe stress analysis, and analysis of 28" cryostat and top plate. This review provides the basis for many of the safety features and measures incorporated in this experiment.

Subsequent to this review and in preparation for the large grain testing program, a C-AD engineering and safety review was conducted in May 2011, and another LESHC-PCSS review in January of 2012. The PCSS review covered the specific of the experimental setup and procedures for conducting the experiment. The action items from this review included pressure analysis of the sapphire viewport, and preparation of standard operating procedures for the large-grain test (included as an appendix to this report).

3 Experimental Method

3.1 Preparation and Cooling

A series of measurements of the RF properties of the cold cavity was conducted starting in May 2012. For each measurement, the preparation and cooldown procedures were roughly the same with greater proficiency and understanding of the practical details of the process achieved in each trial.

To begin, RF cables were connected to the RF ports on the cavity, including the pickup ports on either side of the cavity as well as the FPC port. Throughout the course of testing increasing care was taken to allow sufficient length in the cables to make sure that the connectors at the ends of the cable were not stressed during insertion of the cavity into the cryostat. Furthermore, the route of the cable to the fundamental power coupler was carefully considered to allow the cable to move and shift with minimum strain and interference as the power coupler was moved.

In subsequent experimental trials, due to failures in initial tests (described later in this report), connectors were checked for integrity using a metrology-grade connector gauge (Maury Microwave Model A020D) when possible to make sure connectors dimensions were within the appropriate specification for each connector. In addition, each RF cable was checked using time-domain reflectometry (TDR) both before the cable was connected to the cavity and after connection to make sure that the cables were properly connected.

Next, the cavity assembly, including the top plate and baffle plates with the cavity suspended below the plates was hoisted into the cryostat and the top plate was bolted to the top of the cryostat. The cryogenic fill lance was then inserted into the top plate and the cryostat was rolled into the SVTF.

Once the cryostat was rolled into place, the cables for the pressure sensors, ion pump, RF cables, temperature sensors, heater, and, in later experiments, the camera data cable, were connected to the ports on the top plate, along with the vacuum manifold piping for the cryostat. This manifold piping allowed for regulation of the cryogen pressure inside the cryostat, in turn, providing the

means necessary for changing the temperature of the helium cryogen as well. Figure 3.1 shows the port assignments at the top plate allowing for all of the experimental equipment.

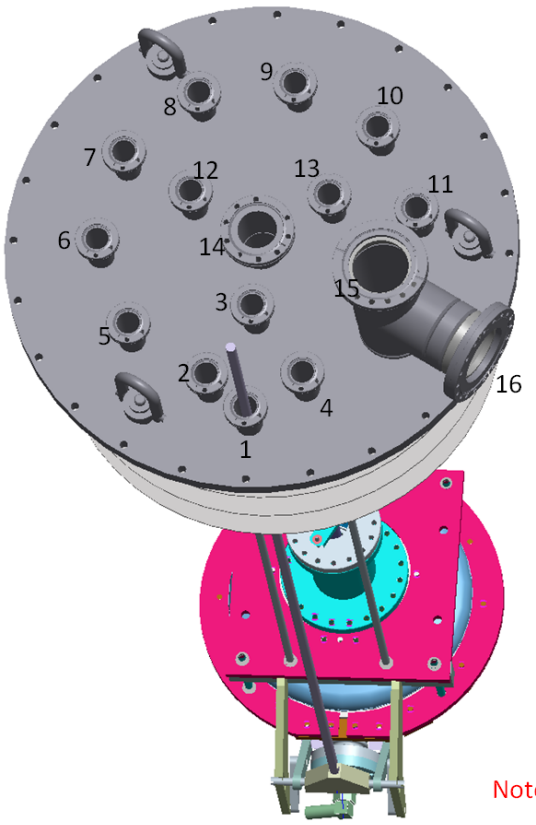

1. Actuator Drive
2. Pickup probe feedthrough - 2
3. *No through holes in baffle plates - unusable*
4. RF coupler power feed
5. Level sensor
6. Fill lance
7. Pickup probe feedthrough
8. Second (working) level probe
9. *Hindered due to ion pump - limited usability - avoid*
10. Camera
11. Temperature sensor feedthrough
12.
13. *Hindered due to burst disk - unusable*
14. Cavity vacuum pumpout
15. Dewar pumpout and relief
16. -

Lee, 5/16/13
Note: 2, 10 & 14 also have internal flanges.

Figure 3.1 - Schematic of port allocations on top plate for large-grain experiment.

The cryostat features an insulating vacuum jacket, and the pressure inside the jacket was measured as part of the cooldown preparation. The jacket pressure was maintained at no greater than 27 microns and, in general, lower pressures were achieved and maintained throughout the cooldown in order to make sure that cooling of the cavity was as efficient as possible.

The transfer line from the storage dewar to the cryostat was then connected via a vacuum-jacketed transfer tube. The coupling between the inserted fill lance and the cryostat was made via a bayonet connection and, as a practice, the vacuum jacket of the transfer tubing inside the SVTF was evacuated using a turbo pump prior to transfer of the liquid helium into the cryostat. A diagram illustrating the features of the transfer line is given in Figure 3.2.

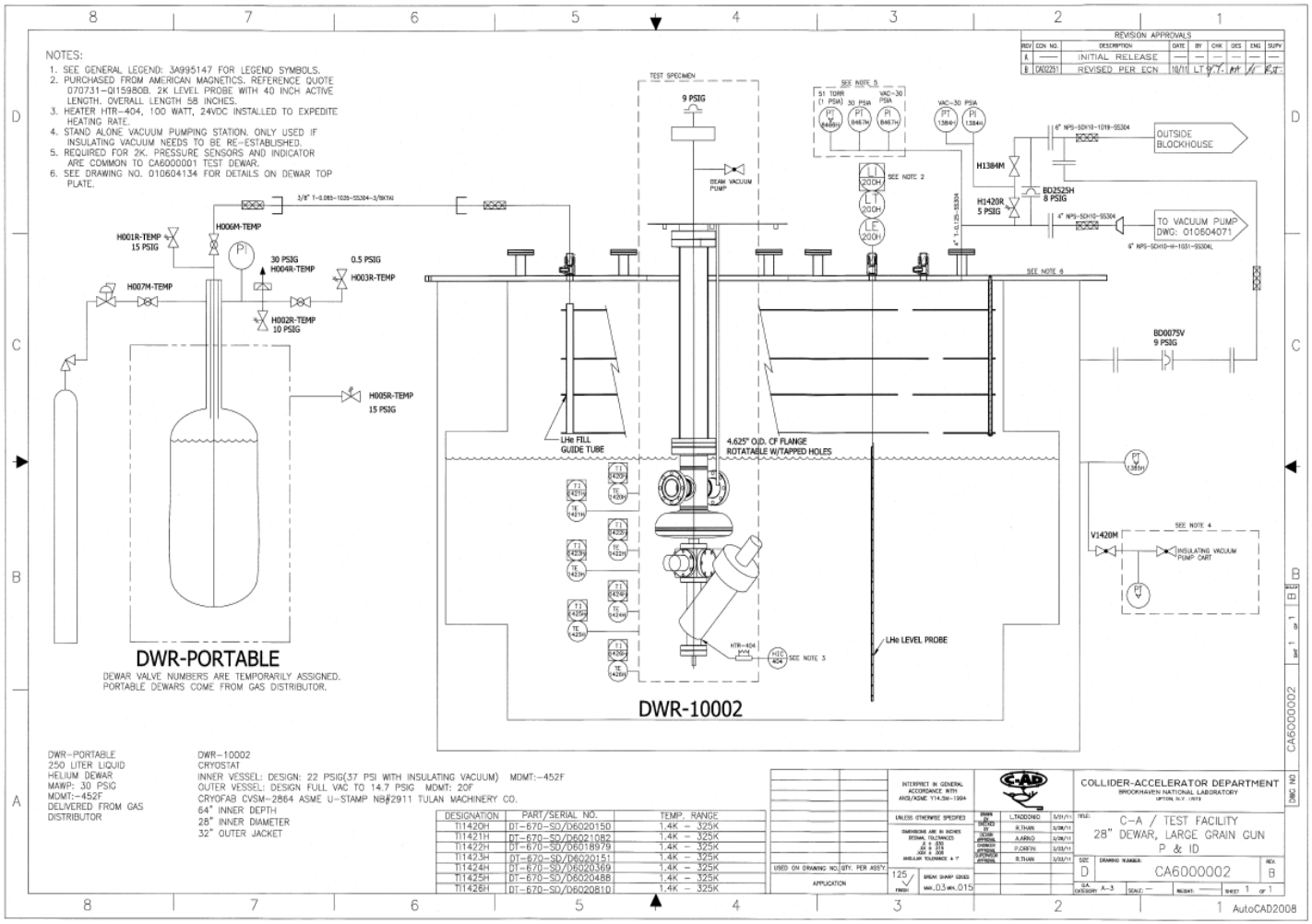

Figure 3.2 - Helium transfer process and instrumentation diagram for the Small Vertical Test Facility. Note that the diagram does not depict the large-grain cavity.

After the transfer line was mated with the cryostat fill lance and prior to transfer of liquid helium, a pump and purge cycle was completed, purging the cryostat of air while pumping warm helium gas into the vessel in order to prevent freezing of air and water vapor components in the transfer line of the cryostat. This process was conducted for approximately one hour.

Furthermore, with the addition of the camera chamber it was necessary to pump down the chamber volume and ensure the pressure was no more than 1×10^{-3} T (the limit of the sensor measurement range) using a turbo pump. At this point, the camera volume was sealed using the valve for the chamber on the top plate. The vacuum pressure of both the cavity and the camera chamber were then noted to assure vacuum integrity. Vacuum pressure in the cavity generally ranged from 10^{-9} to 10^{-10} T depending on the trial at this point in the preparation process.

Next, cavity cooling commenced as liquid helium was transferred from the storage dewar into the cryostat. Because of the small diameter of the vacuum-jacketed transfer line, the transfer rate was quite slow and required anywhere from 2 to 3 days to complete transfer of the liquid depending on the level of helium desired and the cooling requirements. The weight of the supply dewar was regularly measured in order to monitor the rate of transfer and the supply dewar was eventually pressurized up to ~10 psi maximum in order to maintain the transfer.

The transfer conditions were monitored using temperature probes arrayed throughout the experimental apparatus. In addition, a level probe was also used to monitor the helium level. However, because the probe did not extend all the way to the bottom of the dewar, the temperature sensors were used initially as the primary monitor of the transfer and cryogen depth until the level reached the probe. A schematic showing the dimensions of the probe relative to the cryostat is shown in Figure 3.3. It should also be noted that the original level probe used for the experiment had to be replaced after a malfunction that could not be repaired despite several attempts.

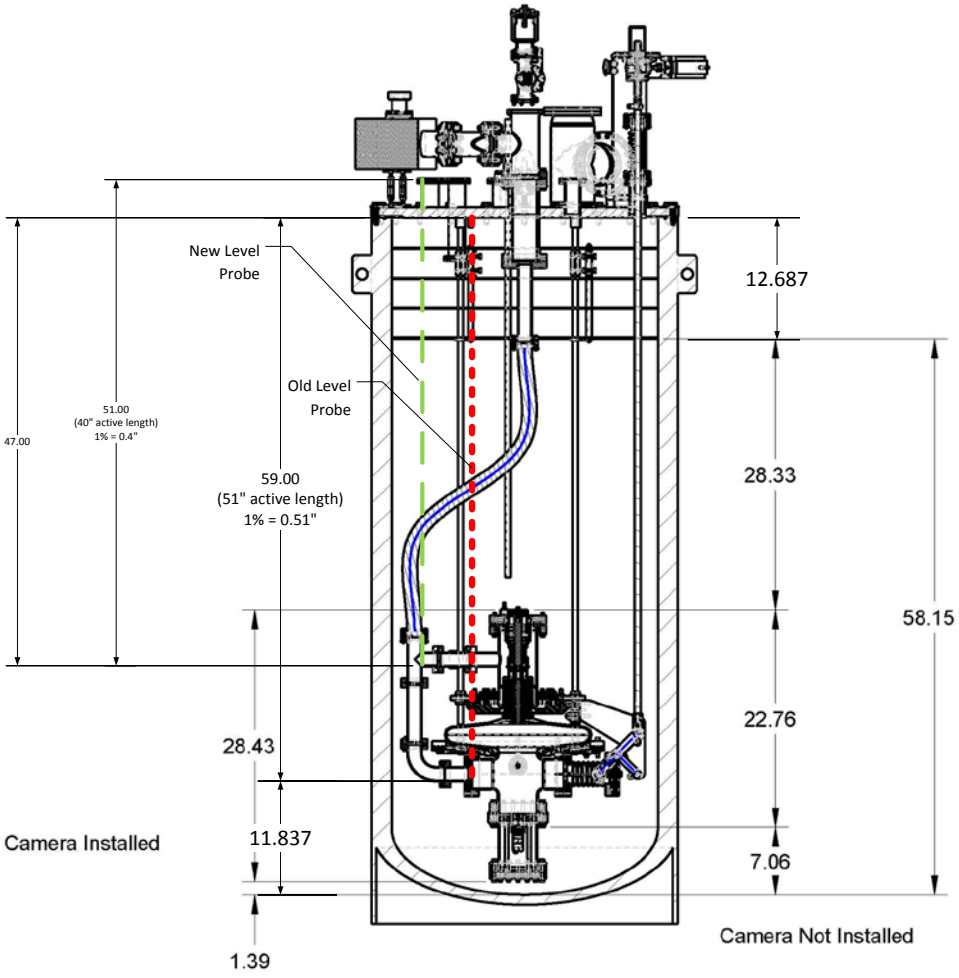

Figure 3.3 - Schematic showing placement and depth of level probes. The line marked "Old Level Probe" shows the depth of the original level probe. The line marked "New Level Probe" shows the depth of the replacement probe. Note that foam inserts directly underneath the top plate and around the camera chamber are not shown.

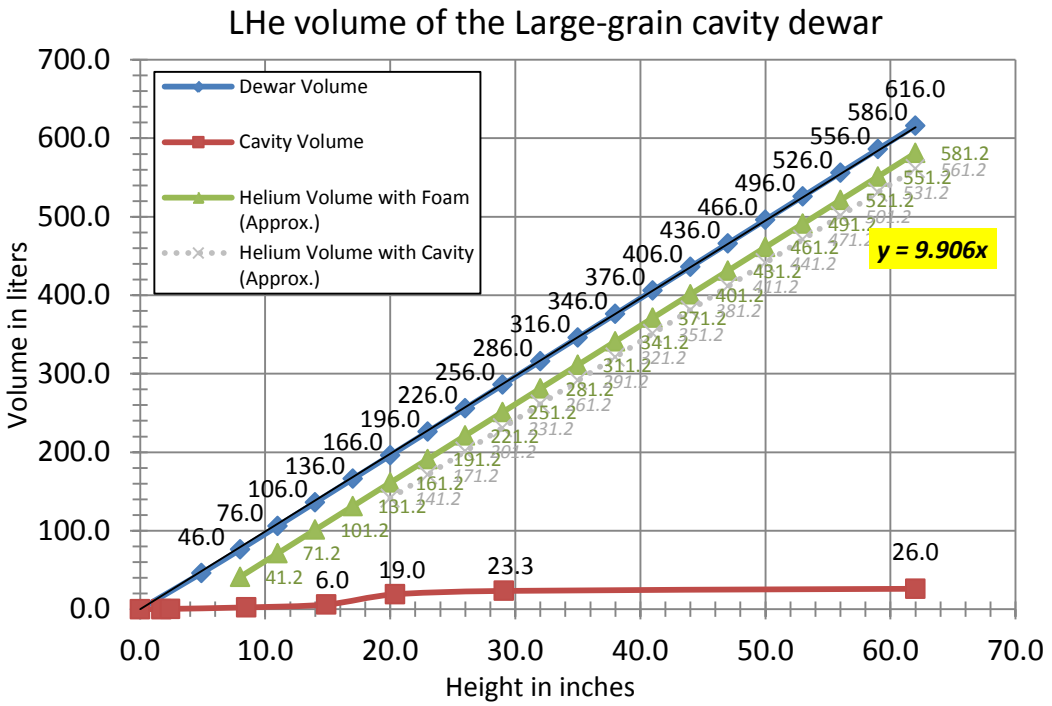

Figure 3.4 - Plot showing estimated volumes of helium in dewar for various heights of liquid. The plot also shows the volumes occupied by the experimental apparatus including the cavity and foam placed underneath the cavity.

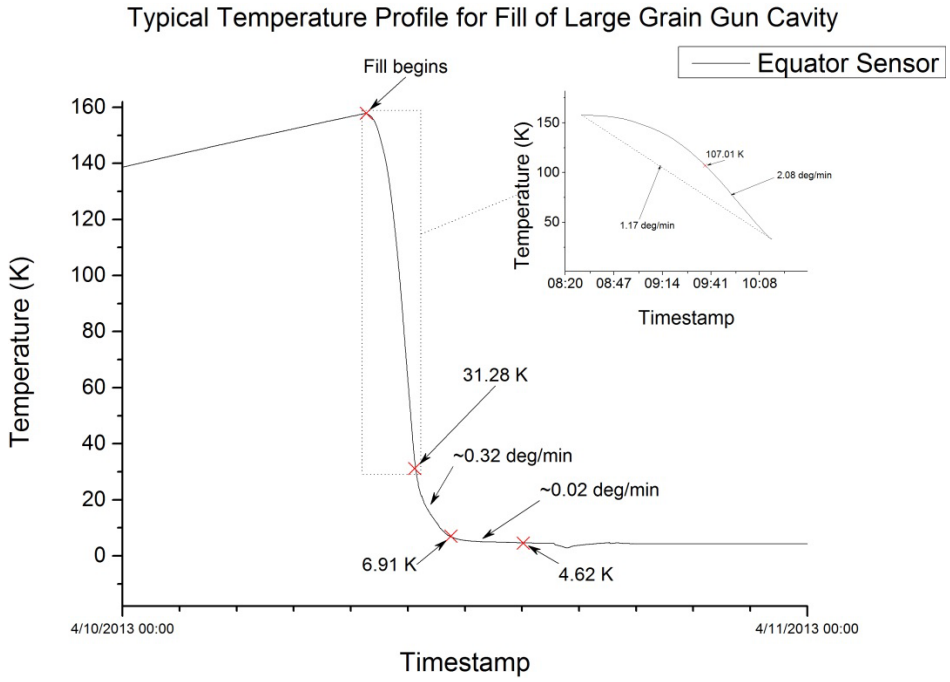

Figure 3.5 - Typical temperature profile for transfer of liquid helium to cryostat. The inset details the change in temperature from the beginning of the fill to 31.28 K.

The fill continued until all of the sensors registered ~4 K and the level probe registered ~55%. This placed the helium level within about 6" of the lowest baffle plate. Figure 3.4 shows a plot with the estimated helium volume for given heights included. The chart shows that for a 55% reading on the level probe, the volume of cryogen in the cryostat reached about 456 L. This level was not always consistently achieved before beginning measurements, particularly for the preliminary RF measurements of the cavity, but for the later measurements including the final measurements cited later in this report, a 55% fill was the goal before beginning the measurement. A typical temperature profile and cooling of the cavity and measurement is given in Figure 3.5.

3.2 Power Measurements

Power measurements of the forward, reflected, and transmit signals were conducted using the configuration and devices outlined in the RF System section. Power was measured using the Boonton 4300 RF power meter. The basic outline of the measurement system is expressed in Figure 3.6.

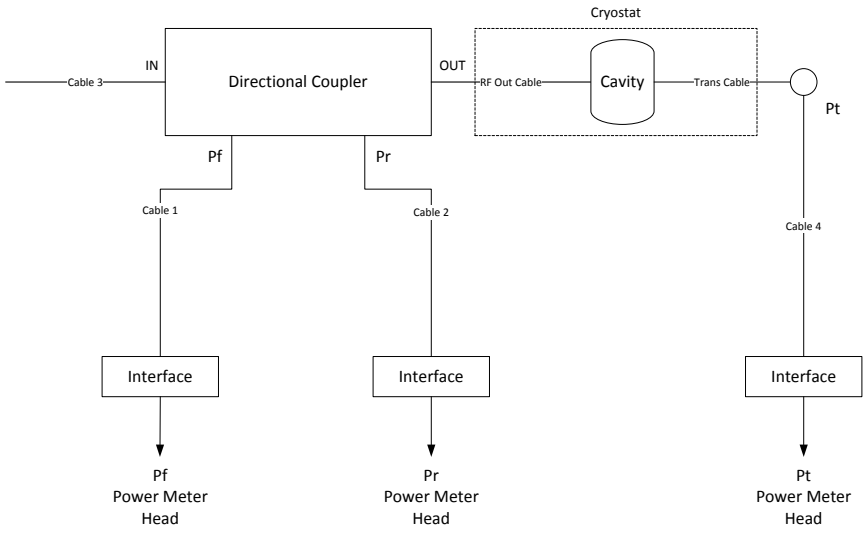

Figure 3.6 - Schematic diagram of measurement system.

Then, based on this diagram, the following expressions for power were applied:

$$P_f[dBm] = P_{f\_meas} + Att_{f\_cable3}[dB] + Att_{dir\_coupl\_f}[dB] - Att_{dir\_coupl\_insert\_loss}[dB] - Att_{RF\ Out\ Cable}[dB] \quad (3\text{-}1)$$

$$P_r[dBm] = P_{r\_meas} + Att_{r\_cable3}[dB] + Att_{dir\_coupl\_r}[dB] + Att_{interface} + Att_{RF\ Out\ Cable}[dB] \quad (3\text{-}2)$$

$$P_t[dBm] = P_{t\_meas} + Att_{Trans\ Cable}[dB] + Att_{t\_cable4}[dB] \quad (3\text{-}3)$$

where P_f is the forward power, P_r is the reflected power, P_t is the transmitted power. A table of values for each of the quantities in the expressions appears below for the final set of test measurements. Of course, it is necessary to measure components inside the cryostat when the cryostat is cold. This includes the *RF Out* and *Trans* cables.

Table 1 - Calibration Factors for RF System

	Attenuation Cable 3 [dB]	Attenuation Dir. Coup. [dB]	Attenuation PLL/Interface [dB]	Attenuation Dir. Coup. Ins. [dB]	Attenuation RF Out Cable [dB]
Forward	2.754	31.182	2.01	13.71	0.07
Reflected	0.07	31.377	9.95		2.11
Transmitted	0.178	3.26	20.52		

Then, the power delivered to the cavity and the power loss in the wall is given by

$$P_{delivered}[W] = P_f[W] - P_r[W], \tag{3-4}$$

and

$$P_{loss}[W] = P_f[W] - P_r[W] - P_t[W] \tag{3-5}$$

3.3 Coupling and Q Measurement

Power measurements were conducted at various input power levels in order to determine the coupling of the fundamental power coupler to the cavity, the voltage achieved in the cavity, and both the loaded and intrinsic Q of the cavity at both 4 K and 2 K temperatures. The intrinsic Q of the cavity is found by first determining the loaded Q of the cavity as well as the coupling. The loaded Q, in turn, is determined by measuring the decay constant of the cavity. Since,

$$P_r = \frac{4\beta^2}{(1+\beta)^2} P_i e^{-t/\tau} \tag{3-6}$$

where β is the coupling constant, a measurement of the reflected power during transient conditions allows the cavity time constant τ to be determined. Therefore, τ was measured by switching off the input power to the cavity and recording the signal on an oscilloscope. The oscilloscope data was then fitted using an exponential fit algorithm. For the measurement, the fundamental power cou-

pler was withdrawn to its farthest point from the cavity to insure the cavity remained under-coupled. Then,

$$Q_L = 2\pi f_0 \tau \tag{3-7}$$

where f_0 is the resonant frequency of the cavity.

Measurement of the power also allows for measurement of the coupling. Now,

$$\beta_{FPC} = \frac{Q_0}{Q_{FPC}} = \frac{1 \pm |\Gamma|}{1 \mp |\Gamma|} \tag{3-8}$$

where Q_0 is the intrinsic Q of the cavity, Q_{FPC} is the external Q of the fundamental power coupler, and Γ is the reflection coefficient, such that,

$$0 \leq |\Gamma| = \left|\frac{V_r}{V_f}\right| \leq 1 \tag{3-9}$$

and

$$|\Gamma| = \sqrt{\frac{P_r}{P_f}}. \tag{3-10}$$

The upper sign is for the over-coupled case, and the lower sign is for the under-coupled case. To determine the nature of the coupling, the coupler was moved incrementally, observing the change in P_r until P_r was minimized. The minimum of P_r indicated critical coupling ($\beta = 1$). The coupler position was measured in volts obtained from a potentiometer attached to the drive system to measure the displacement of the coupler as described in the *Fundamental Power Coupler Design* section earlier in this report.

With the coupling, the Q_{FPC} can be calculated:

$$Q_{FPC} = Q_L \frac{\beta_{FPC} + 1}{\beta_{FPC}}. \tag{3-11}$$

This value is then used to calculate the voltage in the cavity:

$$V_c = \frac{\beta_{FPC}}{\beta_{FPC} + 1} \sqrt{4P_f \cdot R/Q \cdot Q_{FPC}} \tag{3-12}$$

as well as the external Q of the pickup:

$$Q_{PU} = \frac{V_c^2}{P_t \cdot R/Q} = \frac{P_f}{P_t} Q_{FPC} \left(\frac{\beta_{FPC} + 1}{\beta_{FPC}} \right)^2 . \tag{3-13}$$

Then, the intrinsic Q is given by,

$$Q_0 = \left[\frac{1}{(\beta_{FPC} + 1) \cdot Q_L} - \frac{1}{Q_{PU}} \right]^{-1} \tag{3-14}$$

4 Results

4.1 Coupling Measurement and Adjustment

In general, the fundamental power coupler was adjusted to obtain $\beta = 1$. However, at 4 K, it was found that critical coupling was not possible to achieve. A plot of coupling at 4K appears in Figure 4.1.

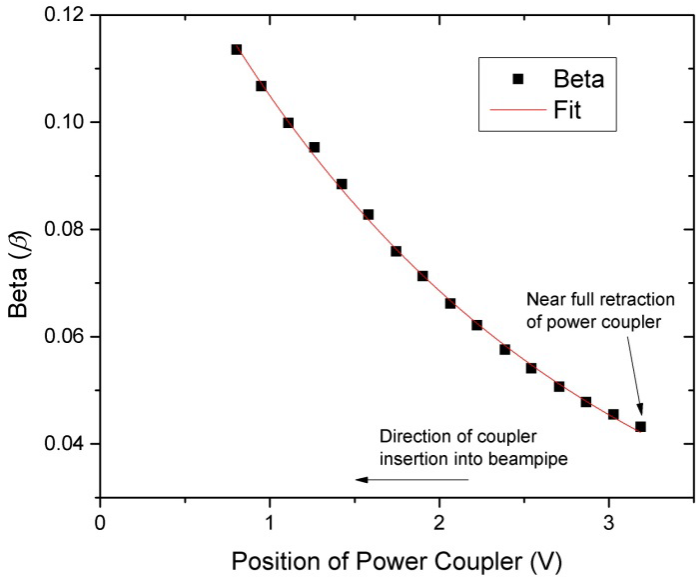

Figure 4.1 - Plot of coupling (β) versus coupler position at 4 K. The position of the coupler is given as a voltage from a linear potentiometer.

Note that the coupler reaches its maximum insertion point at the leftmost portion of the plot. The weakness of the coupling at this insertion depth was unexpected and will require further analysis. Figure 4.2 shows a plot of the accompanying power levels for the measurement using the 20 W amplifier.

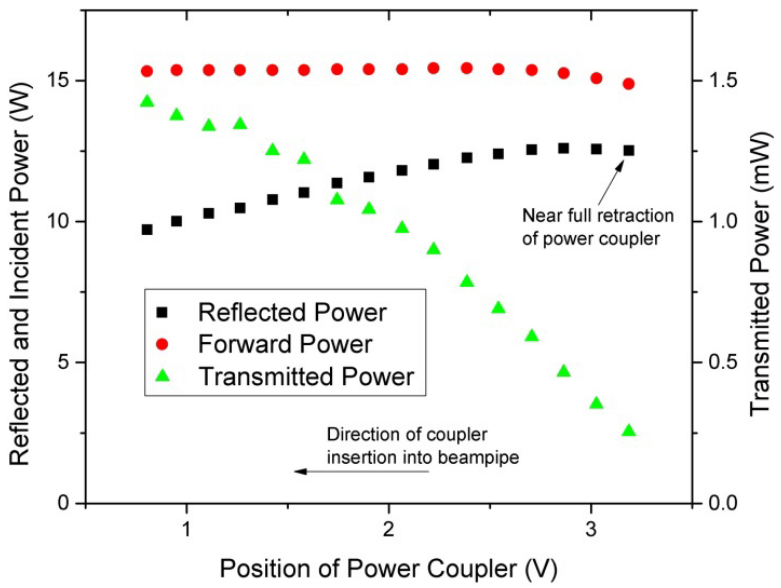

Figure 4.2 - Reflected, forward, and transmitted power at 4 K using 20 W amplifier.

At 2 K, critical coupling was achievable at a variety of power levels. Critical coupling was verified in each case by adjusting the coupler and minimizing the reflected power level at each input power level. A plot of the position for each forward power level is giving in Figure 4.3.

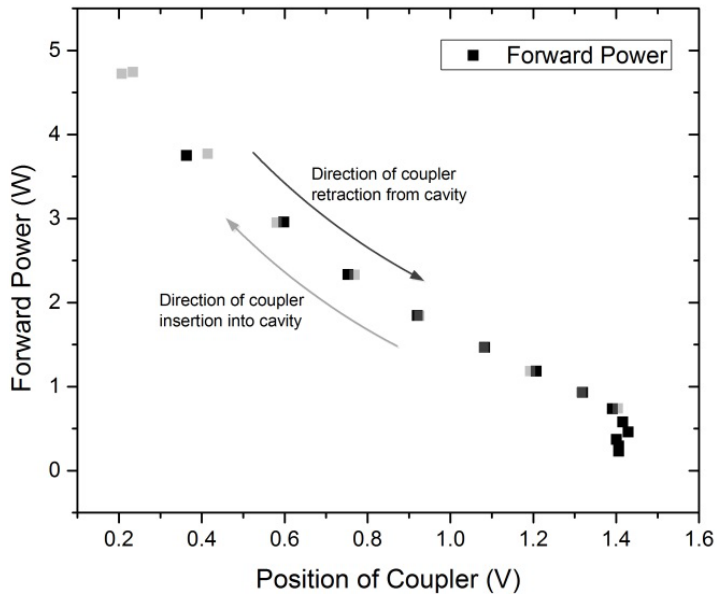

Figure 4.3 - Forward power versus coupler position in volts for cavity at critical coupling ($\beta = 1$). Note that beyond about 0.2 V, critical coupling is no longer achievable. Black dots show power as coupler is retracted from cavity, grey dots show power as coupler is inserted into cavity.

4.2 Time Constant Measurement

The results for the measurement of the constant at both 4 K and 2 K are given in Figure 4.4 and Figure 4.5. The time constant was measured using the decay of the reflected power signal after shutting off the RF while the cavity was significantly undercoupled. At 4 K, the time constant was found to be 0.09207 s and at 2 K, the constant was 0.65861 s.

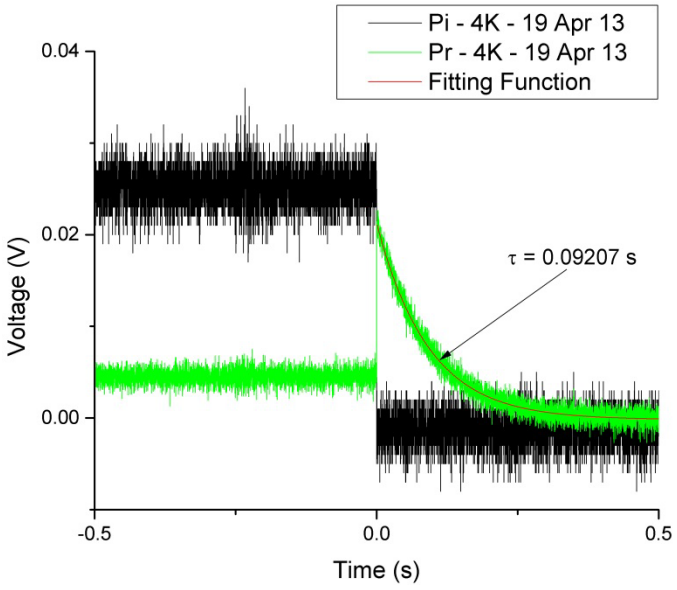

Figure 4.4 - Measurement of incident power (P_i) and reflected power (P_r) from cavity during rapid switch-off of RF at 4K to determine cavity decay constant.

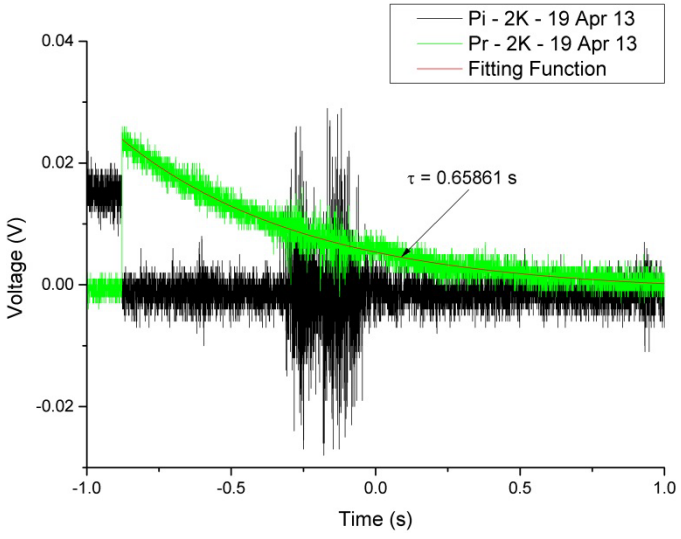

Figure 4.5 - Measurement of incident power (P_i) and reflected power (P_r) from cavity during switch-off of RF at 2K to determine cavity decay constant.

4.3 Multipacting

Throughout the course of testing the large grain cavity, only one significant multipacting level was encountered at a rather low power level of ~4 W at a voltage of 2.41×10^4 V in the cavity. This required about two hours of pulsed processing and was easily overcome. No multipacting in the cavity was predicted in simulations, and none was directly observable through the camera. It seems likely that this was multipacting at the power coupler.

4.4 Q vs. E Measurement

The results for measurement at both 4 K and 2 K temperatures are given in Figure 4.6. The results show that the cavity was able to achieve a voltage of about 0.6 MV before the Q of the cavity begins to roll off significantly. This voltage achieves a Q of $\sim 6.0 \times 10^9$ at 2 K with a frequency of 704.469 MHz and $\sim 6.5 \times 10^8$ at 4 K with a frequency of 704.109 MHz. These Q values are about a factor of 10 lower than the expected Q performance for a cavity of this type. Note that field emission also begins to become appreciable at 0.6 MV and thereafter rises significantly, clearly indicating that Q is limited by field emission. This, in turn, may indicate cavity contamination likely during assembly of the experiment.

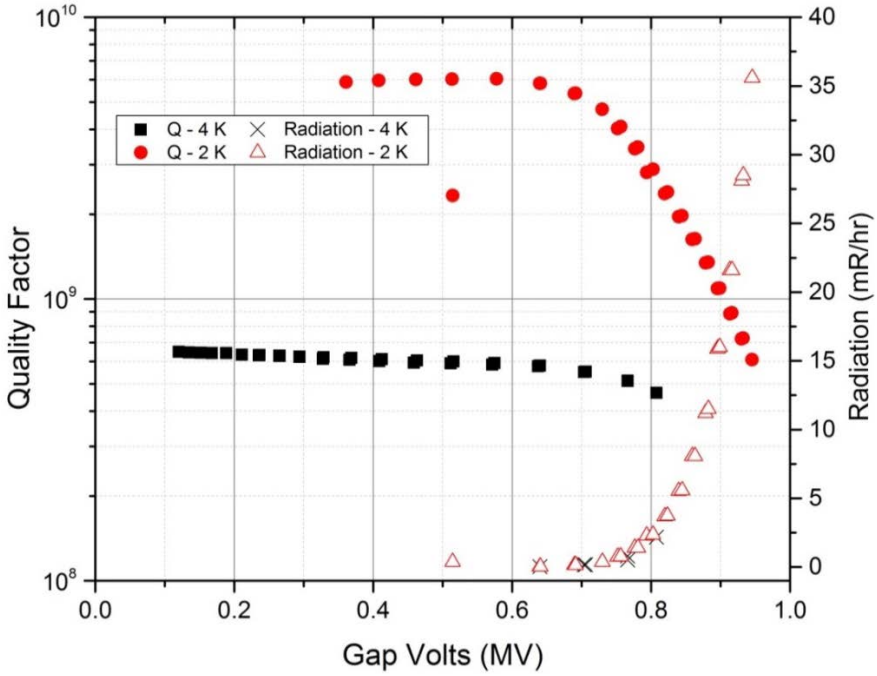

Figure 4.6 - Measurement of quality factor (Q) versus field in the cavity at both 2 K and 4 K temperatures. The radiation from field emission is also shown with its axis on the right of the plot. Field emission increases significantly above 0.7 MV in the cavity, likely indicative of contamination in the cavity.

In the context of these results, it is also interesting to calculate the surface resistivity the cavity based on the field data. Recall that

$$U = \frac{1}{2}\mu_0 \int_V |\mathbf{H}|^2 dV \tag{4-1}$$

and

$$P_c = \frac{1}{2}R_s \int_s |\mathbf{H}|^2 ds. \tag{4-2}$$

Then,

$$Q_0 = \frac{\omega_0 U}{P_c} = \frac{\omega_0 \mu_0 \int_V |\mathbf{H}|^2 dV}{R_s \int_s |\mathbf{H}|^2 ds} = \frac{G}{R_s} \tag{4-3}$$

where, R_s is the surface resistance and G is the geometry factor. Now,

$$G = \frac{\omega_0 \mu_0 \int_V |\mathbf{H}|^2 dV}{\int_s |\mathbf{H}|^2 ds}. \tag{4-4}$$

Since the large-grain cavity is a half-cell structure, we assume a G of 112.7 Ω. The theoretical surface resistance is given by the expression,

$$R_s = A\omega^2 \exp\left(-\frac{\Delta(0)}{k_B T}\right) \tag{4-5}$$

where $\Delta(0)$ is the energy gap between the superconducting and normal states at T = 0 K, k_B is the Boltzmann factor, and A is the slope of the surface resistance as R_s approaches the residual resistance R_0. As Padamsee explains [9], the expression approximates the value of R_s when $T < T_c/2$ when $\Delta(T)$ has reached the asymptotic value $\Delta(0)$. The R_s can also be approximately using (4-5). So, the value of A can be approximated by considering the surface resistance at two different temperatures. Then,

$$A = \left(R_{s\,(4K)} - R_{s\,(2K)}\right)\left[\omega^2 \exp\left(-\frac{\Delta(0)}{k_B T_{4K}}\right) - \omega^2 \exp\left(-\frac{\Delta(0)}{k_B T_{2K}}\right)\right] \tag{4-6}$$

$$\frac{A}{\omega^2} = \left(R_{s\,(4K)} - R_{s\,(2K)}\right)\left[\exp\left(-\frac{\Delta(0)}{k_B T_{4K}}\right) - \exp\left(-\frac{\Delta(0)}{k_B T_{2K}}\right)\right]. \tag{4-7}$$

The value of R_s, R_{BCS}, and R_0 are given below in Table 2. Note that the residual resistance of ~17 mΩ is somewhat large and suggests that additional etching of the surface may be profitable for the overall performance of the cavity.

Table 2 - Table of Resistance Values at Various Temperatures

Temperature	R_s [Ω]	A	R_0 [Ω]	R_{BCS} [Ω]	R_{BCS} [Ω] (Padamsee) [9]
4 K	1.74×10^{-4}	4.53×10^{-5}	1.67×10^{-8}	1.57×10^{-7}	1.53×10^{-7}
2 K	1.92×10^{-8}			2.48×10^{-9}	2.41×10^{-9}

The role of additional energy losses was also explored in simulation studies by J. Dai to account for the low Q of the cavity. In particular, losses in both the bellows and the camera chamber were explored. The bellows and the camera chamber are made of stainless steel. Energy losses were simulated using CST Microwave Studio, and the model is shown in Figure 4.7.

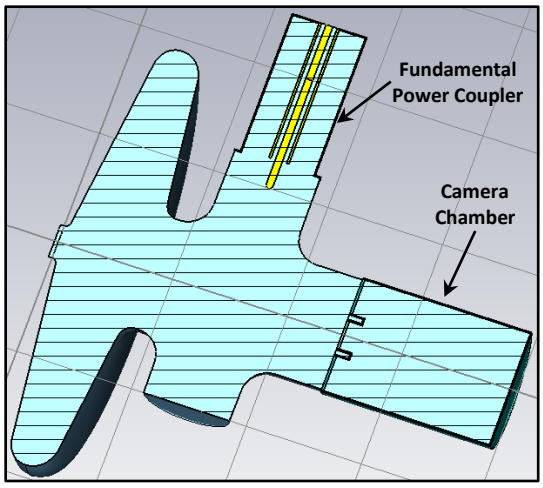

Figure 4.7 - CST Microwave Studio model used to determine RF losses in both the coupler bellows system, at the top of the model, and in the camera chamber, to the right of the model. The bellows are composed of stainless steel and interfaces with the cavity via a copper gasket. Furthermore, the coupler itself is composed of copper. The camera chamber is also stainless steel with a copper gasket as well as a sapphire window in the center.

Furthermore, the maximum insertion point for the coupler is shown in Figure 4.8. The results of the simulation are presented in Table 3. The table shows the normalized energy losses for both copper and stainless-steel as well as copper alone for various positions of the coupler relative to the cavity flange. In Table 4, the total energy stored in the cavity as calculated from the experimental measurements is shown along with the percentage of loss as calculated from simulation relative to the total energy. The points included in the table are at the full insertion point at the coupling (1.05 inches) and about midway between the flange and the maximum insertion point (0.87 inches).

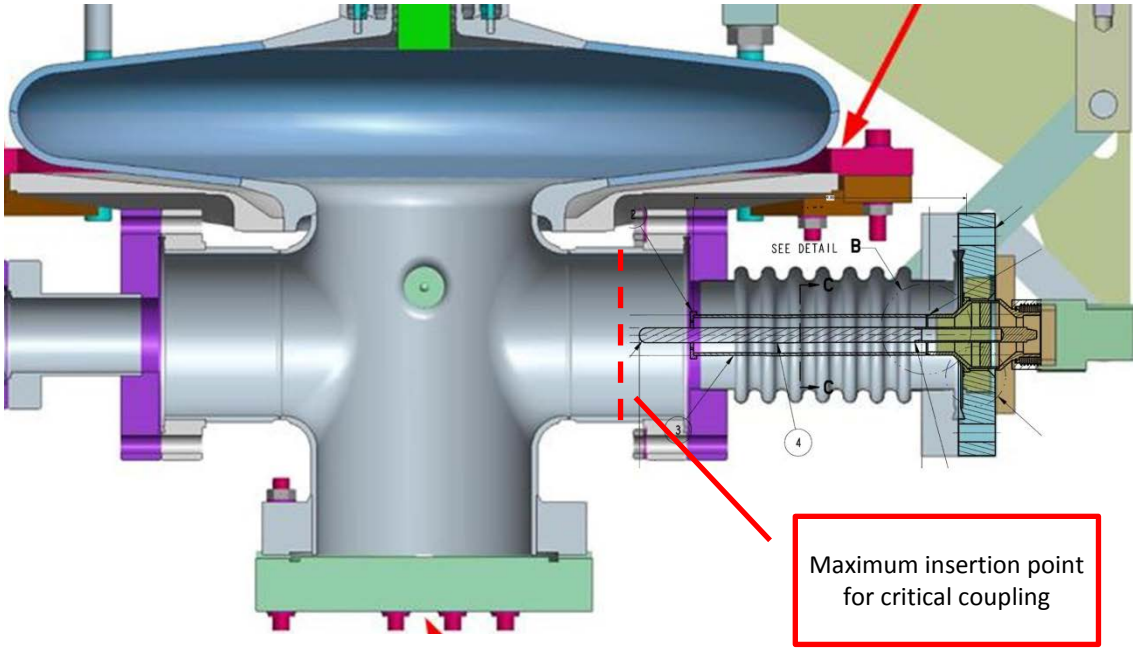

Figure 4.8 - Schematic showing maximum insertion point for the fundamental power coupler into the cavity. Recall that critical coupling was only achieved at 2 K.

Table 3 - Simulation of Losses in Large Grain Cavity (Stored Energy: 1 J)

Tip Position [in]	Loss in Cu [W]	Loss in Stainless Steel [W]	Total Loss for Cu and Stainless Steel [W]
0.87	5.42×10^{-4}	1.74×10^{-2}	1.79×10^{-2}
1.05	8.49×10^{-4}	2.01×10^{-2}	2.09×10^{-2}

Table 4 - Calculation of Total Energy and Energy Loss from Experimental Measurements

Tip Position [in]	Q_0	Stored Energy [J]	Total Loss [W]	Normalized Total Loss [W]	Percentage of Total Loss for Cu and Stainless Steel (from simulation)
0.87	2.13×10^9	1.22	2.54	2.08	8.62×10^{-3}
1.05	1.86×10^9	2.78	6.59	2.37	8.84×10^{-3}

The results of the simulation suggest that only a very small portion of the energy lost in the structure is due to the energy lost in the copper or the camera chamber (less than 0.011%). This also contributes to the supposition that both field emission and surface preparation are the most significant factors in the performance of the cavity.

Taking into account all of these considerations, the testing project will implement the necessary changes and proceed to the second phase of the project in which the effect of the cathode will be studied. For this phase, a copper cathode with anti-multipacting grooves will be inserted into the cavity choke joint and the effect will be studied. Preparations are underway for this phase of the experiment.

4.5 Camera Results

In this phase of the experiment, no multipacting was expected to be visible and none was observed on the camera. However, inclusion of the camera at this stage was important to test the configuration and operation of the camera.

These tests were highly successful and produced very clear, sharp images throughout operation. The camera was operated continuously during testing, meaning that the camera was required to function for many days at a time and procedures good images throughout. The camera was trained on the blank flange at the opposite end of the cavity, sealing the top hat of the experimental assembly. A picture of the camera mounted and outfitted with LEDs for illumination in the cavity appears in Figure 4.9 and an example of a typical image from the camera appears in Figure 4.10.

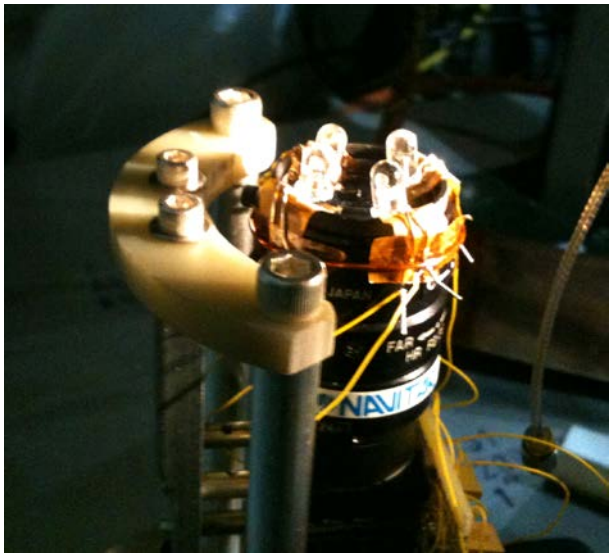

Figure 4.9 - Camera mounted on support before insertion into the camera chamber, showing arrangement of LEDs at the front of the camera.

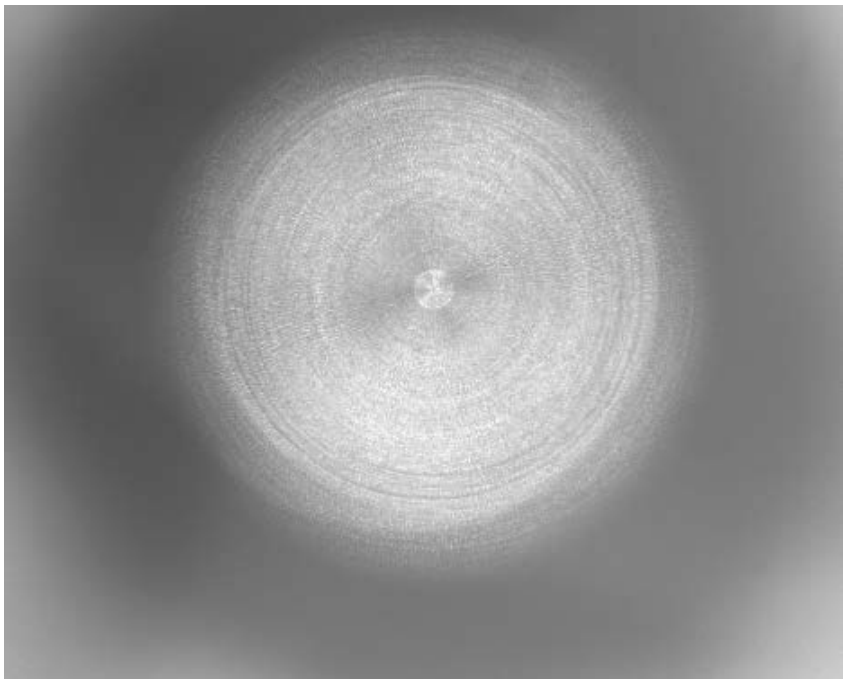

Figure 4.10 - Typical camera image during testing. The camera is focused on a blank flange 19" away from the camera looking through the gun cavity. The image is illuminated by four LEDs attached to the front of the camera.

The only time that camera operation was significantly impaired was during those moments when the highest field emission was observed, essentially blinding the camera due to the high radiation field. Fortunately, the camera was able to recover from these junctures and continue to produce images with field emission reduced and no significant degradation in image quality or performance was subsequently observed.

5 Operating Experience and Lesson Learned

5.1 Slow Transfer of Helium

Lesson: Future efficient operation of both the large-grain experiment and SVTF will require a larger transfer line in order to make the various experiments more efficient and to avoid the potential to suffer *Q*-disease due to a slow rate of cooling.

One of the most significant difficulties in operating the experiment was the amount of time required to transfer helium into the cryostat and cool the cavity. Filling the cryostat required several days and, in general, was extremely slow. The clear cause of this extended filling time was the small diameter of the transfer line. In addition, at various points in the course of operation, icing along portions of the fill lance was encountered due to inadequate pump out of the vacuum jacket of the fill lance.

This issue has already been addressed and a new transfer line has been designed, procured, and installed. A schematic of the new transfer line is given in Figure 5.1.

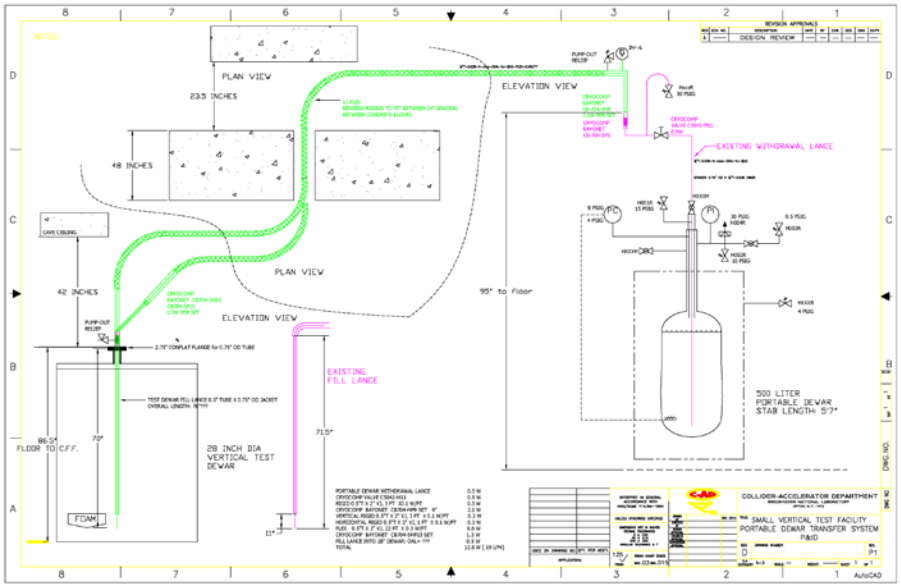

Figure 5.1 - Schematic of new helium transfer line for the Small Vertical Test Facility.

5.2 Cable Failures

Lesson: Preparation of the test requires careful attention to the preparation and measurement of the cables. Cable failures due to loose or improperly prepared connectors proved to be problematic in several instances causing test delays and failures. The situation became particularly problematic under the cryogenic conditions of the test.

The first of these cable failures occurred due to the initial choice of cable for the fundamental power coupler. This was a rather large cable intended to carry kilowatts of power from the klystron used in the ERL. However, the initial testing would only involve a 20 W amplifier and therefore the larger cable was unnecessary even for subsequent 200 W testing. It became evident that the cable was a poor choice because the motion of the cable, attached to the fundamental power coupler, combined with the stiffening of cable, contributed to loosening of connectors in the feed line, ultimately compromising the test. The cable was replaced with a more appropriately-sized cable and, at the same time, emphasized the need for taking additional quality assurance measures such as checking all cable connections with time-domain reflectometry to ensure sound connections, particularly in the environment of the helium bath.

After one such failure, the changes that might occur to N-, SMA-type, and 7/16”-DIN-type connector dimensions were carefully studied under cold-shock testing conditions. SMA-type connections are used at the RF pickup of the cavity while N- and 7/16”-type connectors are used at the fundamental power coupler as diagrammed in Figure 5.2. The adapter and the elbow are manufactured by Pasternak, Inc. SMA- and N-type connectors were manufactured by Andrew, a subsidiary of CommScope, Inc.

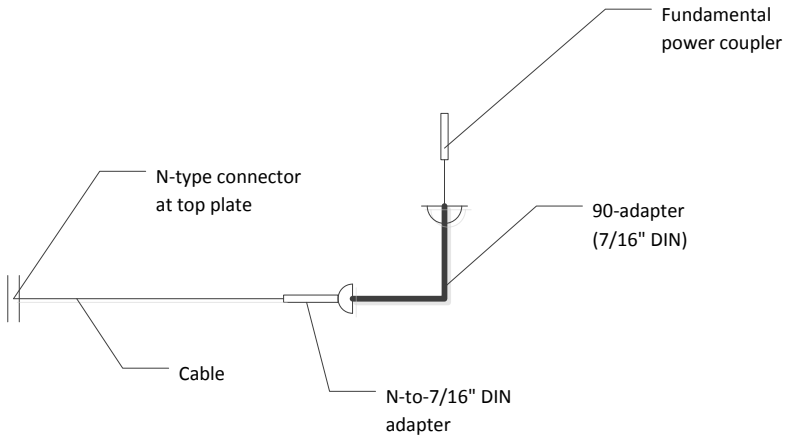

Figure 5.2 - Schematic of connectors used in power coupler circuit (not shown to scale).

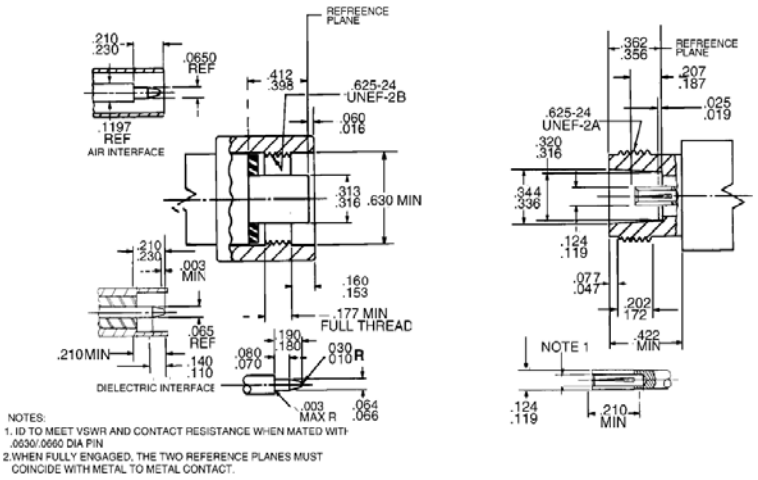

Figure 5.3 - Dimensions for N-type connector. [10]

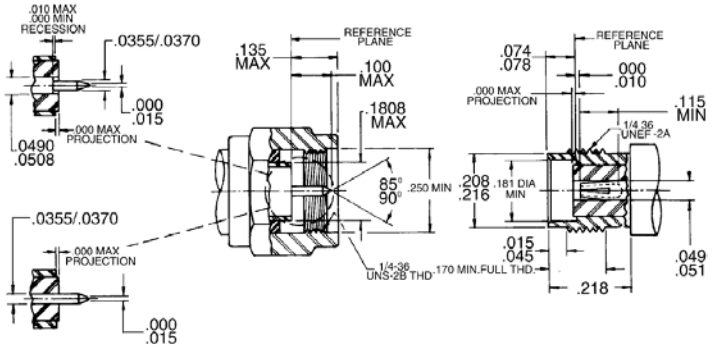

Figure 5.4 - Dimensions for SMA-type connector. [11]

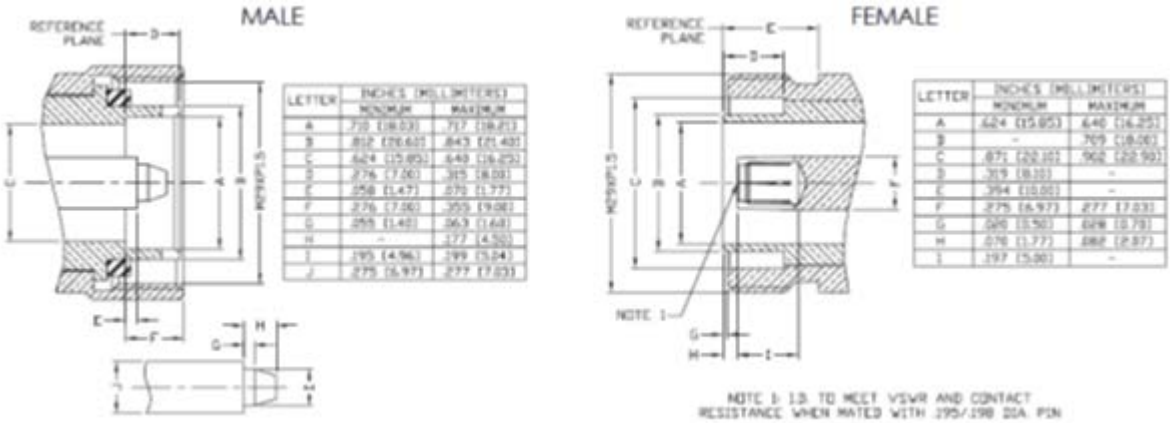

Figure 5.5 - Dimensions for 7/16" DIN connector. [12]

Cables with SMA-type connectors along with an N- to 7/16”-DIN type adapter and a 7/16”-DIN type elbow were measured at room temperature at various locations around the critical dimensions of the connector as shown in Figures 5.2, 5.3, and 5.4; and the dimensions were averaged. Measurements were conducted using a hand-fashioned apparatus not specifically designed for this type of measurement, contributing in some cases to rather large error bars. The cables and the adapter were submerged in liquid nitrogen for approximately 1 hour, removed, and the critical dimensions were measured. This process of cold-shocking was repeated two more times, and then the cables and the adapter were allowed to warm up to room temperature and were measured for one last time. The measurements are shown in Figures 5.5, 5.6, 5.7, and 5.8. The results show that the dimensions of the N- to 7/16”-type adapter changed very little (1-2%), and the changes remained well within the connector specifications. Upon warm-up, the connector roughly returned to its original dimensions before cold-shocking. It is interesting to note, however, that the SMA connectors did not return to their original dimensions after cold-shocking. This suggests that these connectors must be handled with particular care since their dimensions may fall outside of the connector specification with repeated use. These connectors must be reinspected before each use and, for greater reliability, should likely be changed to a different type of connector.

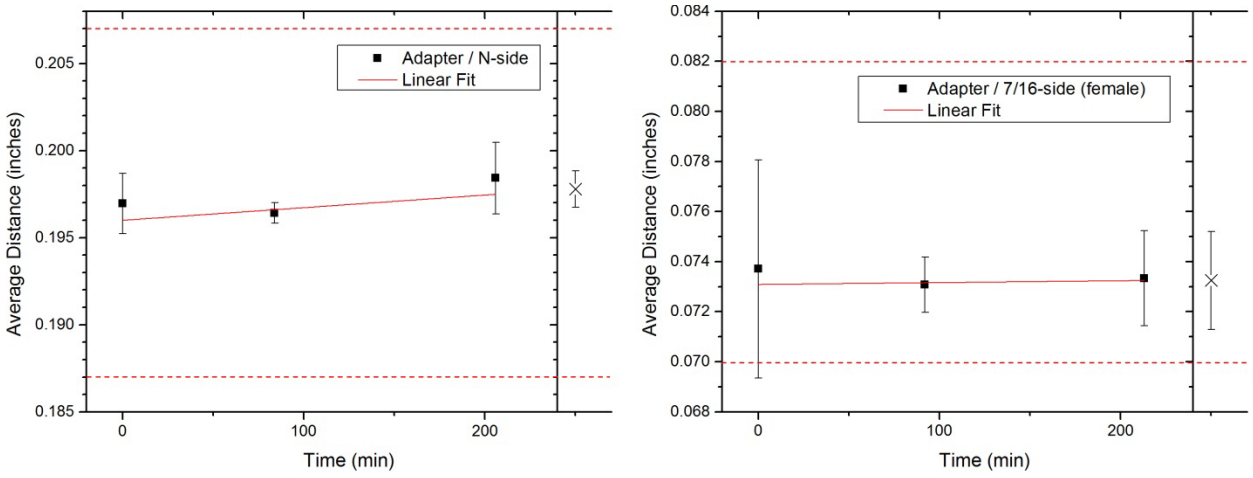

Figure 5.6 - Measurement of dimension from reference plane to inner-conductor-tip at N-type side and 7-16”-type side of straight adapter in power coupler circuit. The last data point to the far right of each plot shows the last dimension measurement after warmup. Dotted lines at top and bottom of each plot show the specification range for the connector dimension.

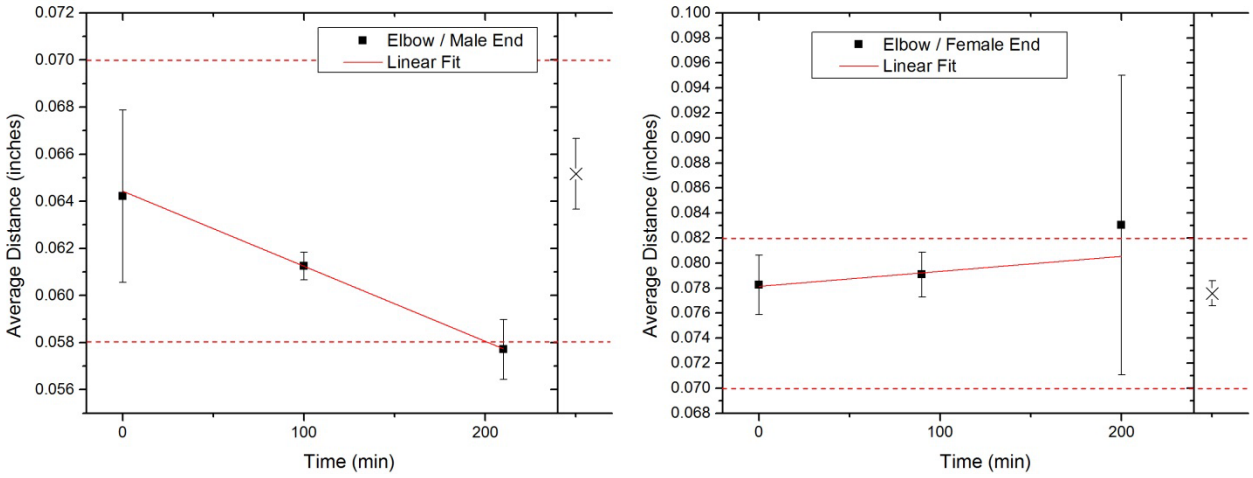

Figure 5.7 - Measurement from reference plane to inner-conductor tip in 7/16" DIN connector in elbow adapter of power coupler circuit. The last data point to the far right of each plot shows the last dimension measurement after warmup. Dotted lines at the top and bottom of each plot show the specification range for the connector dimension.

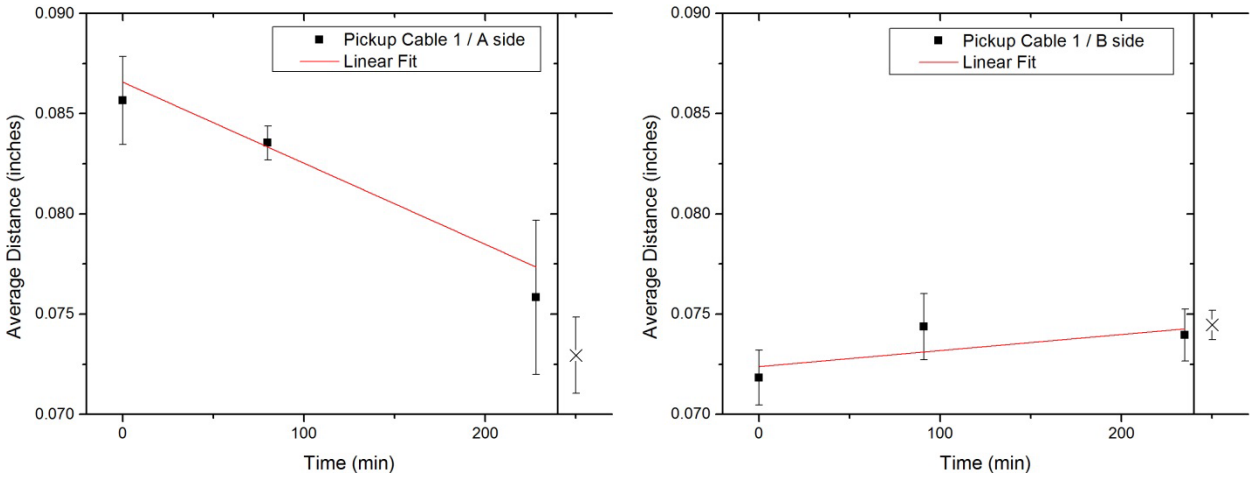

Figure 5.8 - Measurement from reference plane to inner-conductor tip in SMA connector of pickup cable. The last data point to the far right of each plot shows the last dimension measurement after warmup. The plot range encloses the specification range for the connector dimension.

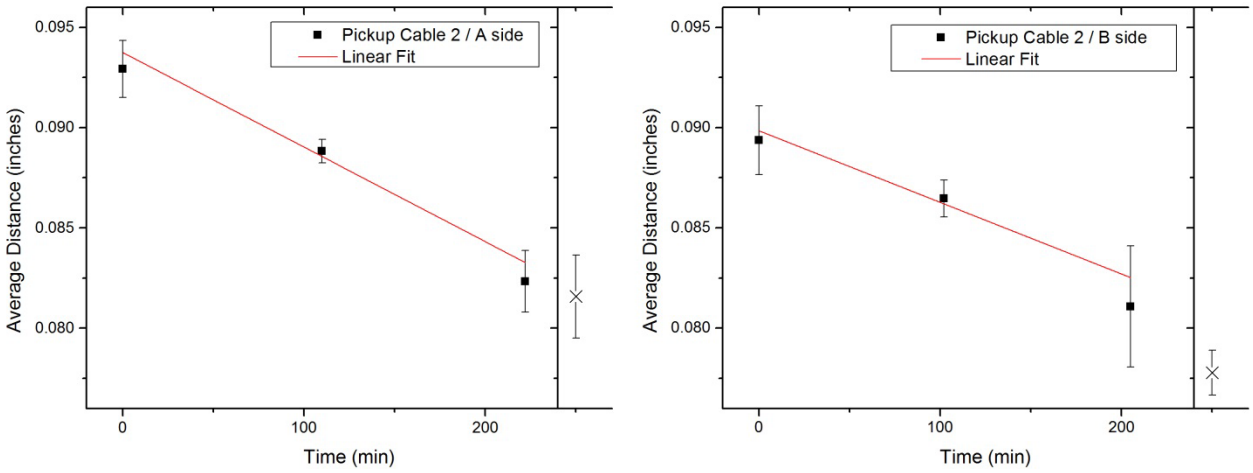

Figure 5.9 - Measurement from reference plane to inner-conductor tip in SMA connector of pickup cable. The last data point to the far right of each plot shows the last dimension measurement after warmup. The plot range encloses the specification range for the connector dimension.

5.3 RF System Reconfiguration

Lesson: The phase-locked loop system must be reconfigured with new components so that the maximum power from the 200 W amplifier used for the experiment can be utilized. The system was limited because it had not originally been designed to use a 200 W amplifier but rather a 20 W amplifier.

As the testing program proceeded, it was decided to use a larger amplifier, but the system was not sufficiently reconfigured to allow for the larger amplifier. New components will be required to fully accommodate the larger power requirement before the next test.

5.4 Cleanroom Assembly

As the testing program proceeded, it was decided to use a large amplifier, but the system was not sufficiently reconfigured to allow for the larger amplifier. New components will be required to fully accommodate the larger power requirement before the next test.

While every effort was taken to work as cleanly and carefully as possible, this was the first time that some of those principally involved in assembly had worked on a project of this type. The considerable experience gained in this effort will benefit future assembly work.

6 Plans for Future Testing

Having successfully completed the first stage of testing and understanding changes and improvements required in the experimental setup, the next stage of testing will focus on understanding the nature of multipacting in the cavity. A copper cathode has been fabricated and will be inserted into the cavity in order to test the effect. Both the copper cathode and the cavity have fresh grooves of the intended geometry.

An important focus at this stage is the effect of groove alignment on multipacting. Simulation results by J. Dai indicate that alignment of grooves plays a crucial role within the choke joint. In the simulations, the effects of the altered geometry on both the cathode and the cavity were studied as well as the alignment of the grooves relative to each other.

In Figure 6.1, the multipacting in two "pristine" surfaces are compared. In this case, multipacting is observed for various misalignments *except* for 4L/8 and 5L/8 where L is the spacing between grooves. In addition, no multipacting is observed when there is no misalignment. Indeed, when there are no misalignments, the results of previous multipacting studies performed by W. Xu [3], indicate that the altered geometry of grooves exposed to chemistry contributes to multipacting as shown in Figure 6.2. Taken together, these studies suggest that if there is no misalignment and the surfaces are triangular, no multipacting is expected to occur. However, if the surfaces are rounded, multipacting can be expected to occur, even if the surfaces are aligned. Dai's work, however, adds an important caveat: if the surfaces are misaligned in certain ways, multipacting can be expected to occur, even if the surfaces are triangular.

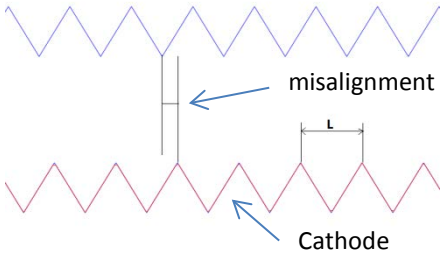

(a)

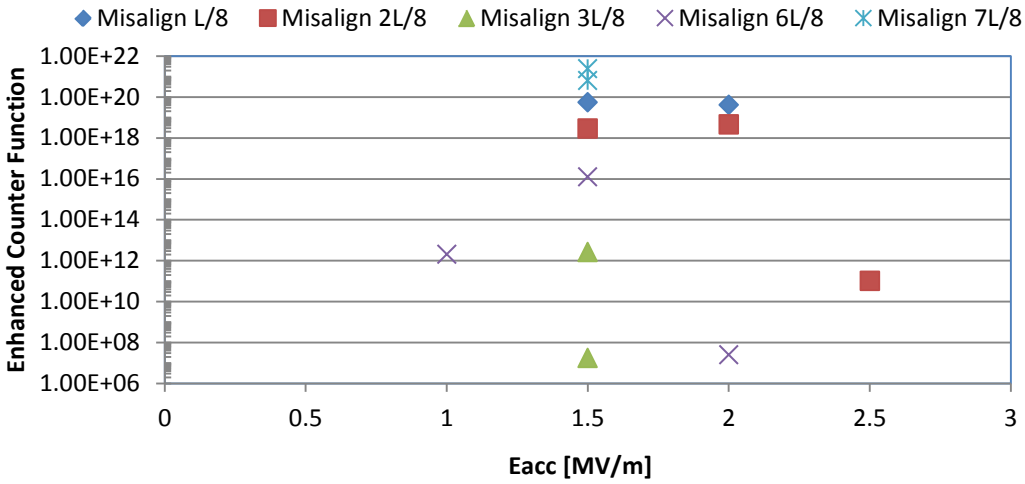

(b)

Figure 6.1 (a) - Cartoon of misalignment between the "pristine" (triangular) surfaces of the cavity and the cathode stalk. The width of each groove is L. (b) – Enhanced counter function for multipacting simulation at various misalignment intervals. No multipacting is observed for misalignment intervals of 0, 4L/8, and 5L/8. Note that the enhanced counter function value is maximal for L/8 and 7L/8.

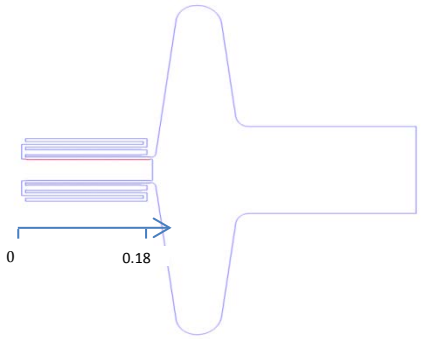

(a)

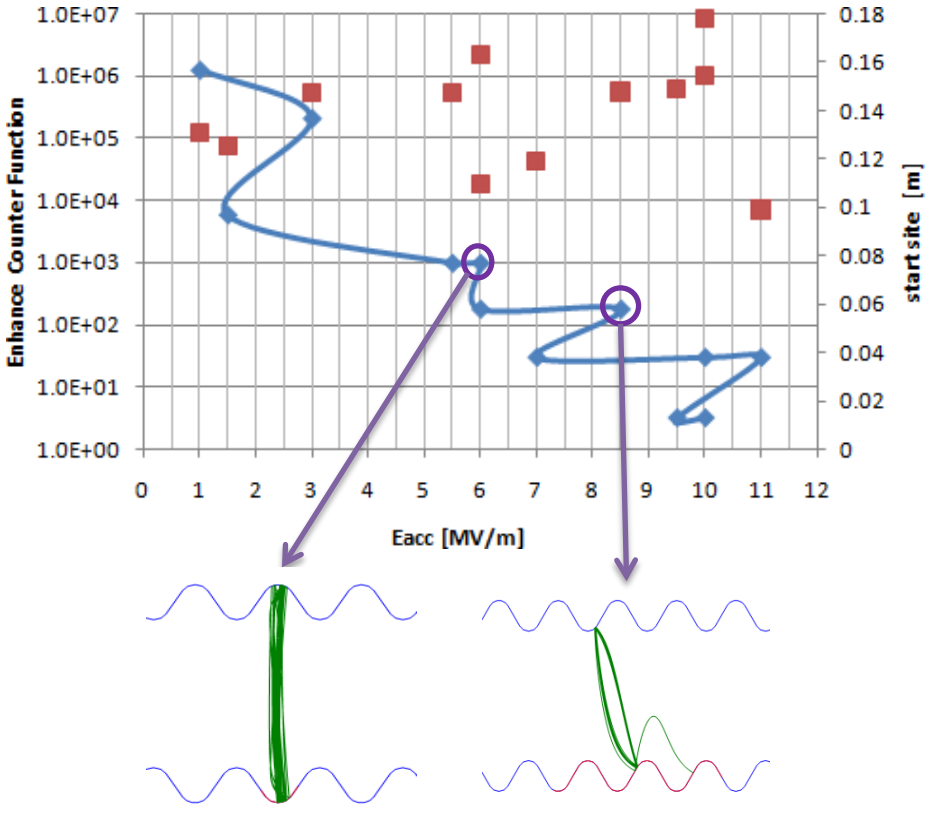

(b)

Figure 6.2 (a) - A cartoon of the cavity showing the choke joint as well as the portion of the cavity that was considered for the simulation. (b) - Enhanced counter function values for grooved surfaces with altered geometry. The grooves are 1 mm wide, and two types of multipacting phenomena are shown to occur for grooves that are aligned peak to peak. The blue curve shows the various sites, in terms of distance from the end of the choke joint toward the cavity, where the enhanced counter function is highest. (0.18 m is closet to the cavity, 0 m is furthest away from the cavity, at the edge of the choke joint.) The red dots indicate the value of the enhanced counter function. The counter function is highest further away from the cavity where the field in the choke is highest [3].

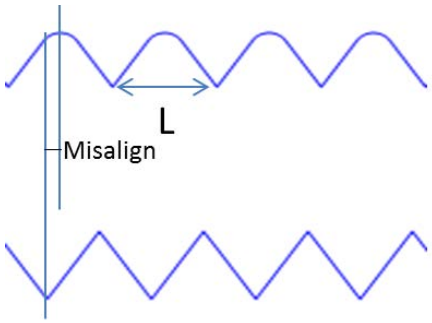

(a)

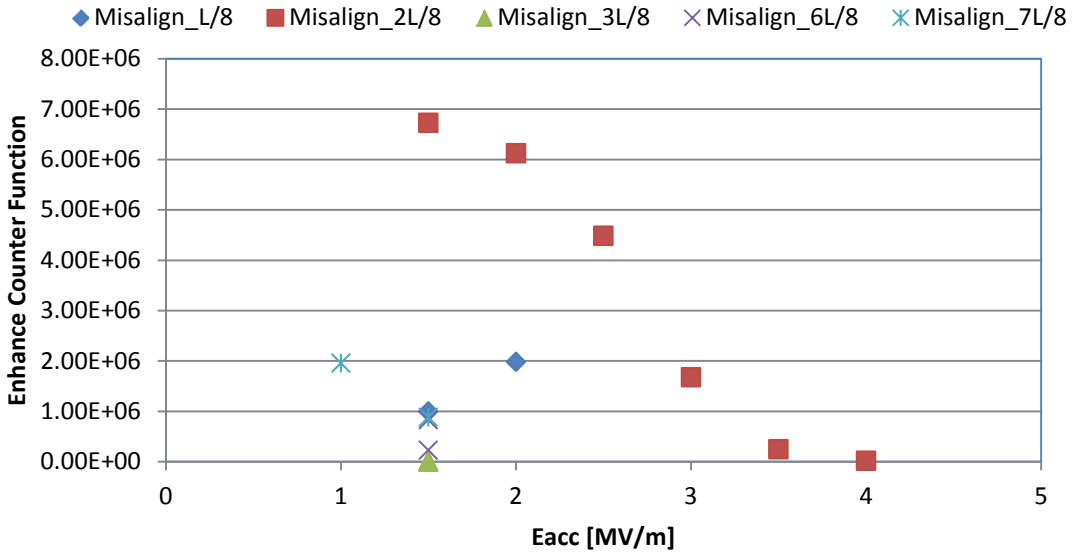

(b)

Figure 6.3 (a) - Cartoon showing misalignment between altered surface and "pristine" triangular surface. The groove width is L. (b) – Plot of enhanced counter function for various alignments. Note that no multipacting is observed for 8L/8, 4L/8, or 5L/8. The maximum counter function value occurs for 2L/8.

Figure 6.3 shows the simulation result when the actual situation is considered: a "pristine" cathode stalk surface and the altered geometry of the cavity. In this case, the results are the same: no multipacting is observed when there is no misalignment, and when the peaks and valleys of the stalk and the cavity are "anti-aligned". Again, it appears that alignment is the key factor in multipacting, even when the surfaces are triangular. This conclusion from simulation data, in turn, suggests a straightforward test strategy:

1. Insert the cathode into the cavity. Since the state of alignment may be difficult to establish in advance, the precise alignment may be unknown. Watch for signs of multipacting. This will then serve as a reference alignment. Since simulation results indicate that no multipacting should be observed for aligned or "anti-aligned" grooves, no indication of multipacting would suggest an aligned or anti-aligned state.

2. Next, alter the cathode length in such a manner as to alter the alignment by half a groove period (0.5 mm). Simulation predicts that should leave the state of multipacting unchanged. Watch for signs of multipacting.

3. Alter the cathode length by a quarter of the groove period (0.25 mm). Simulation predicts that this should change the state of multipacting. Watch for signs of multipacting.

These steps should allow for confirmation of the simulation predictions. The work also has important implications for the behavior of the gun cavity in the ERL. Should multipacting occur, these experiments may provide an important indication of both the cause of the multipacting as well as a possible solution strategy.

The above strategy will be challenging to implement, however, because of the nature of the cathode. In order to change the alignment, alterations are envisioned to be made at the flange face where the cathode meets the cavity to change the depth of the cathode stalk relative to the cavity. This is shown in Figure 6.4. This flange presents a slender face for removing material, and removal and cleaning of the resulting cathode must be handled carefully in order to prevent particulate contamination of the surrounding grooves, lest these particles become sources of field emission. Furthermore, the cathode is press-fitted to the cavity flange. Changes to the dimensions of the cathode flange may change the nature of the press-fit. These issues must be addressed in the experimental design and engineering.

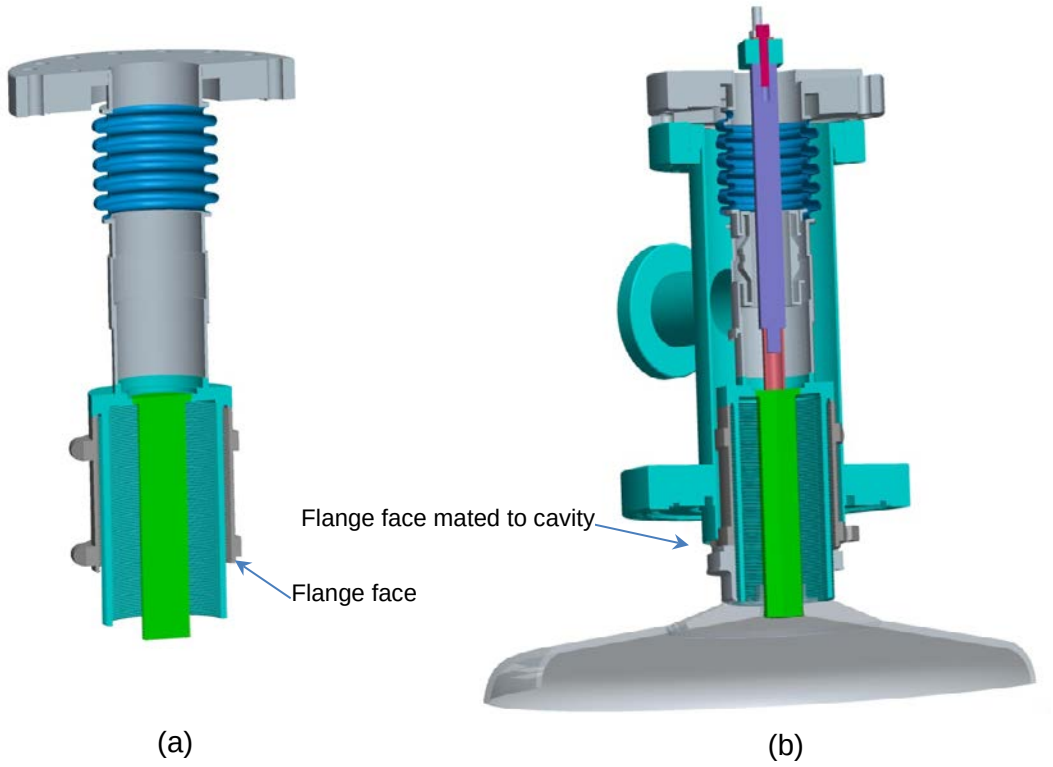

Figure 6.4 (a) - The copper cathode stalk showing the flange face when the stalk is press-fit against the cavity. Note that the cathode is spring-loaded (not shown) to hold the cathode against the cavity face. (b) The cathode mated with the cavity. Note that that the cathode shown in (b) reflects an older design that was changed for the current series of experiments. (a) shows the actual design of the cathode. (b) shows the spring-loaded shaft that fits through the center of the cathode.

7 Conclusions

This report has discussed the experimental details and results of the first stage of testing the large-grained niobium superconducting half-cell structure identical in geometry to the gun cavity used in the Energy Recovery LINAC currently under construction. The design considerations behind each of the component parts of the experiment have been discussed and, where appropriate, specific upgrade recommendations are given along with lessons learned. In many cases, these upgrades are already underway, are being developed, or have been completed, paving the way for additional testing stages.

The principal goal of the first stage of testing was to prove the experiment components and configuration as well as to test the basic RF properties of the cavity. In addition, this experiment also commissioned a new test facility in Building 912, The Small Vertical Test Facility. Given these goals, testing was largely very successful. The basic design of the experiment ultimately allowed for measurement of the cavity after a period of learning how best to cool the cavity, how to properly handle helium transfer to the cryostat, correcting cable troubles that contributed to substantial delays, and determining how to configure the low-level RF system. The most significant problems with the experiment arose from the limitations of the transfer line, the configuration operation of the low-level RF System, and the design of behavior of the drive system for the fundamental power coupler.

In addition, the results of the cavity testing itself appear to point to several process issues during assembly that should be evaluated and addressed in subsequent work. These include evidence of a preparation process for the cavity that requires optimization as well as subsequent assembly that may have contaminated the cavity.

The narrow helium transfer line caused cooling of the cavity to be very slow. During the early filling efforts, the transfer of helium could take several days to complete, resulting in a highly inefficient process that was costly in terms of helium. It was eventually realized the problems with the diameter of the line, faulty transfer technique, and a vacuum jacket that was not fully evacuated pump contributed to the poor performance of the transfer line. These problems were eventually

corrected and other measures were taken and including addition of foam to the baffle plates as well as ensuring that all vacuum-jacketed components including the cryostat and the transfer line were sufficiently evacuated before beginning the transfer. Furthermore, and most importantly, a new, wider transfer line was purchased and installed that allows for more rapid and efficient helium transfer. The new transfer line also has better valves on the vacuum-jacketed components reducing the need to repeatedly evacuate the jacket and reducing the risk of accidentally spoiling the vacuum jacket.

Cable problems of various kinds contributed substantially to experimental delays and were, ultimately, some of the most troublesome challenges encountered during testing. Some of the effects of the cryogenic environment contributed to these problems and were not properly anticipated. For example, in the initial test, a rather large cable was used to feed power to the fundamental power coupler. This cable was intended to carry kilowatts of power from the klystron used in the ERL. However, only a small amount of power would be used to stimulate the cavity in the initial tests. This would allow for a smaller cable to be used, and the inappropriate choice of cable became problematic in the early stages of testing because the motion of the cable connected to the variable-position of power coupler combined with the stiffening of the heavier cable is believed to have contributed to loosening of connectors in the feed line, ultimately hampering testing.

In the end, the problem prevented testing from continuing and the cable required replacement with a more appropriately-sized cable. Furthermore, the loosening of the connector is emphasized the need to implement appropriate quality assurance procedures that included checking all cables with time-domain reflectometry to ensure sound connections, particularly in the environment of the helium bath.

This experience also compelled us to explore the behavior of the connectors themselves in the helium bath along with the cables. For these reasons, cold-shock testing of the connectors was conducted and data was collected to ensure the reliability of these components. Most all of the components underwent changes in the cold environment that were within their required specifications, but these results once more emphasized the need for careful handling and assembly procedures when using these components in the extreme environment of the helium bath.

Problems in the low-level RF system stemmed from the fact that the system was repurposed from the five-cell cavity for use in the Small Vertical Test Facility. This required some reconfiguration of the components as well as a learning curve to understand how to properly configure and use the

system for stimulating the cavity. At a certain point during testing, it was also decided to add to the original phase-lock loop system a self-excited loop. While the self-excited loop was useful for bringing the cavity into resonance, it required additional time to set up and use. At the end, the phase-lock loop system proved most effective for obtaining experimental data, but all of these systems required a learning curve to optimize their efficient use. Moreover, the phase-lock loop system proved to be limited in its power output because of its design, and components must be reconfigured to allow the full range of the 200 W amplifier to be used. This work will be done before the next test.

The drive system of the fundamental power coupler was also problematic early on due to refinements in the design that were required in the assembly of the experiment. The redesign involved the addition of a reinforcing member to prevent transverse motion of the coupler tip as it moved in and out of the cavity. Several iterations of this reinforcing structure were required in order to prevent binding of the coupler as it moved in and out of the cavity, leading to delays in assembly.

At the end, this redesigned power coupler assembly was successful in reducing transverse play in the copper, but not in eliminating it all together and possibly contributed to a backlash, hampering reproducibility of motion in the coupler to some extent as well as contributing to hysteretic effects. In response, an improved mechanism has been designed to correct these issues and has already been successfully tested in the prototype crab cavity testing program for the LHC.

Finally, the Q of the cavity at 4 K was $\sim 10^8$ and at 2 K was $\sim 10^9$. Both of these values are about a factor of 10 below the expectation for a cavity of this type. This, combined with a calculation of the surface resistance and simulation of potential losses arising from the coupler and the camera chamber suggest that the surface of the cavity may require additional etching. Losses from the coupler and the camera chamber appear to be negligible, and the surface resistance, as calculated from the experimental data, is higher than expected.

Furthermore, the cavity achieves a voltage of 0.6 MV before significant decline in the Q of the cavity occurs along with evolution of high levels of radiation from field emission. The field emission suggests contamination of the cavity most likely having occurred during assembly and requiring additional cleaning of the cavity.

8 Appendix

Procedure for the Vertical Test of the 704 MHz Large-Grain Gun Cavity with up to 200 W Available RF Power

1. Purpose

This procedure covers vertical testing of the 704 MHz large-grain cavity with maximum RF power (CW or pulsed) up to 200 W. A 28" diameter dewar is used for this test. Operation of the dewar is covered in OPM 18.7.3 ERL – Small Test Dewars (14" and 28") Operation.

The vertical dewar test of the 704 MHz large-grain cavity in the Little Block House (LBH) will be carried out in three stages as follows. First, the cavity will be tested without a cathode to check the setup and measure the performance of cavity. Second, a niobium cathode stalk, which was used for the fine-grain cavity test at JLab, will be installed in the cavity and the cavity will be tested to study multipacting that was observed in the fine-grain structure. The RF power available during the first two tests will be limited to 200 W CW or pulsed. Third, a copper cathode stalk will be installed and tested at higher pulsed power (50 kW) to study multipacting further. Average power during the third test will be limited to 200 W.

Note: This procedure covers only the first two tests, which RF power source is interlocked with access control system. The power supply of RF source should be hardwired to the access control system and only access control group has authority to switch the RF sources. The third test with 50kW power source will be covered by a separate procedure.

2. Responsibilities

1) The Liaison Physicist (Sergey Belomestnykh) or the Large-Grain Project Leader (Lee Hammons or Wencan Xu) is responsible for implementing the procedure.

2) Representatives from each involved group (cryogenic, vacuum, RF, PASS) are responsible to make sure that their systems are ready and properly interfaced with other systems.

3) The Operations Coordinator (Dave Pate) or his designee is responsible for confirmation that all paperwork is in order and the system is ready before the test can start.

3. Prerequisites

Before filling the cryostat with liquid helium (LHe) the Liaison Physicist or the Large-Grain Project Leader must make sure that:

1) The RF amplifier is wired as a critical device and interlocked to prevent RF power generation.

2) A logbook is available for logging access procedures.

3) A chipmunk inside the LBH must be operational (*Ck-FY2010-SRF-632*).

4) The door is posted as High Radiation Area (*Ck-FY2010-SRF-635*).

5) Yellow *"Do not operate"* tag should be in places including both ends of all the RF cables, power supply connected to the RF amplifiers, and also the input/output ports of the RF amplifiers.

6) ODH 1 training and a personal oxygen monitor are required to enter the LBH if helium is present (Note: An escape pack is not required since it takes more time to use the escape pack than to leave the LBH.)

7) Ensure that HP has posted area per agreed upon boundary.

8) Two days ahead of time request the cryogenic group to prepare and post the signs and cordon off the area around the blockhouse to warn of startle hazard due reliefs lifting and gas discharging.

9) Arrangements shall be made in advance to test for RF leakage around the perimeter of the Little Blockhouse during the first test. Power levels shall be recorded and evaluated and further action taken if required.

4. Precautions

1) Before starting the experiment, the Operations Coordinator or his designee should make sure that the radiation check-off list and all experimental preparations are complete.

2) If an abnormal condition arises while the sweep is in progress, stop the sweep and discuss the situation with the on-duty CAS Watch or Head of the ESSHQ Division.

3) While sweeping, view over, under and behind equipment for personnel.

4) Do not turn RF power on until the LBH is swept free of personnel and locked. If the maximum power is not higher than 20 mW (the maximum output of the network analyzer is 10 mW), the power source doesn't need to be interlocked and can be used with appropriate precautions by personnel inside LBH.

5) As long as there is liquid He in the Dewar, one has to wait 10 mins with fan on before he/she enters the little block.

5. Emergency shutdown

In the event that a fire alarm goes off in the 912 complex, all non-emergency personnel shall evacuate to outside of the building and await the arrival of the Fire/Rescue Group. The Liaison Physicist (Sergey Belomestnykh) or the Large-Grain Project Leader (Lee Hammons or Wencan Xu) should shut down the RF power source before they leave.

6. Procedure

1) Verify that HP has posted area per agreed upon boundary.

2) Verify that the cryogenic group has posted the signs and cordoned off the area around the blockhouse to warn of startle hazard due reliefs lifting and gas discharging.

3) Ensure that all data loggers (RF, vacuum, temperature) are operational.

4) Begin cryogenic operations. All work related to operating cryogenic equipment (connecting dewars, cooldown, operating pump skid, warmup, etc.) must be performed by the cryogenic

group personnel and should follow OPM 18.7.3: ERL - Small Test Dewars (14" and 28") Operation.

5) Cool down to 4.2 K (or 4.5 K) and establish desired LHe level in the dewar.

6) Calibration at 4.5 K and initial FPC tuning with a network analyzer:

   a) Calibrate the network analyzer.

   b) Measure attenuation of RF cables inside the dewar.

   c) Connect the input coupler and pick-up cables to the network analyzer.

   d) Measure Q_{ext} of PU and FPC coupling range.

   e) Watch S21 and tune the input coupler until the coupler factor is close to 1. The input coupler is tuned using a stepper motor driving the couple via a mechanical linkage.

   f) Calculate calibration coefficients and enter them into a test Excel spreadsheet.

   g) Check calibration of the temperature sensors if necessary.

7) Cool down the cavity to 2 K.

8) Coupling adjustment and *Q* measurement at 2 K:

   a) Re-calibrate the network analyzer if necessary.

   b) Measure attenuation of RF cables inside the dewar.

   c) Connect the input coupler and pick-up cables to the network analyzer.

   d) Measure Q_{ext} of PU and FPC coupling range.

   e) Watch S21 and tune the input coupler until the coupler factor is close to 1. The input coupler is tuned using a stepper motor driving the couple via a mechanical linkage.

   f) Calculate calibration coefficients and enter them into a test Excel spreadsheet.

   g) Restore cable connections at the dewar top plate.

   h) Check calibration of the temperature sensors if necessary.

9) Following the sweep procedure *C-A TPL 11-20: Securing Little Block House for Experimental Tests*, sweep the block house and prepare for operation**.**

10) RF test:

   a) Verify that RF cables are connected to the power source.

   b) Check data logging, low-level RF, vacuum, temperature readings.

   c) Turn on RF power amplifier.

   d) Turn on RF in CW mode at low power level and adjust LLRF parameters for stable PLL . operation.

e) Switch RF to pulse mode, remotely adjust FPC for critical coupling. Use square wave pulse shape to identify coupling.

f) Gradually raise RF power. At each step record forward, reflected and transmitted power, cavity vacuum, radiation inside the block house, LHe level, dewar pressure, cavity temperature, Watch for signs of quench, field emission and multipacting.

g) If necessary, switch to pulse mode to process multipacting or field emission.

h) Stop if limited by quench and pulse processing does not help.

i) Plot *Q* vs. *V* data.

j) Raise RF power to reach the maximum gap voltage.

k) Gradually decrease RF power while at each step recording forward, reflected and transmitted power, cavity vacuum, radiation inside the block house, LHe level, dewar pressure, cavity temperature.

11) Plot *Q* vs. *V* data.

12) Turn off RF and other test equipment.

13) Warm up to room temperature. The access mode should remain "**No Access**" until the the dewar is empty of the LHe and the heater in the dewar is off.

14) Inspect the top plate.

15) If there is no plan to move the cavity, leave everything connected.

16) If the cavity will have to be moved:

17) Turn off ion pumps.

18) Disconnect wires and cables.

19) Transfer the dewar insert to the clean room.

7. References

1. OPM 18.7.3 ERL – Small Test Dewars (14" and 28") Operation
2. C-A TPL 11-20: Securing Little Block House for Experimental Tests
3. RSC Check-Off List for Cold Testing of the 704MHz Large Grain Cavity with Local er Supply

9 Bibliography

[1] Y. Zhao, "Simplified Model of Multipactor Experiment for the Tunnel Dust Choke," Upton NY, BNL-72180-2004-IR, 2004.

[2] L. Hammons and M. Ke, "Measurement of Groove Features and Dimensions of the Vertical Test Cathode and the Choke Joint of the Superconducting Electron Gun Cavity of the Energy Recovery LINAC," C-A/AP/#433, Oct. 2011, Upton NY, 2011.

[3] W. Xu, I. Ben-Zvi, S. Belomestnykh, D. Holmes, D. Kayran, G. Mcintyre, and B. Sheehy, "Multipacting in a Grooved Choke Joint at SRF Gun for BNL ERL Prototype," in *Particle Accelerator Conference (PAC'11)*, 2011.

[4] R. Calaga, "Linear Beam Dynamics and Ampere Class Superconducting RF Cavities @ RHIC," Thesis, State University of New York at Stony Brook, 2006.

[5] R. Calaga, I. Benzvi, M. Blaskiewicz, X. Chang, D. Kayran, and V. Litvinenko, "High current superconducting gun at 703.75MHz," *Physics C Superconductivity*, vol. 441, no. 1–2, pp. 159–172, Jul. 2006.

[6] A. Burrill, "R&D ERL: SRF Electron Gun," Upton NY, BNL-90933-2010-IR, 2010.

[7] P. Anthony, J. Delayen, D. Fryberger, W. Goree, J. Mammosser, Z. Szalata, J. Weisend II, "Experimental Studies of Light Emission Phenomena in Superconducting RF Cavities," SLAC-PUB-13664, July 2009, Menlo Park, CA, 2009.

[8] S. Tuozzolo, "Camera Assembly Design Proposal for SRF Cavity Image Collection," C-A/AP/#434, Oct. 2011, Upton NY, 2011.

[9] H. Padamsee, J. Knobloch, and T. Hays, *RF Superconductivity for Accelerators*, 2nd Edition. Weinheim, Germany: Wiley-VCH Verlag GmbH & Co. KGaA, Weinheim, 2008.

[10] Telemeter-Electronic, "Type 'N' Connectors."[Online]. Available: http://www.telemeter.info/documents/content/8_ksg/n-stecker.pdf.

[11] Telemeter-Electronic, "SMA-Type Connectors." [Online]. Available: http://www.telemeter.info/documents/content/8_ksg/sma-stecker.pdf.

[12] Antenna-Systems-and-Solutions, "7-16 DIN Connector." [Online]. Available: http://antennasystems.com/Merchant2/pdf/Connectors_7-16-DIN.pdf.